Universidad Autónoma de Baja California

Facultad de Ingeniería, Arquitectura y Diseño

Maestría y Doctorado en Ciencias e Ingeniería

Topological Data Analysis of Eye Fundus Digital Images

THESIS

presented to partially fulfill the needed requirements to obtain the degree of

DOCTOR IN SCIENCE

By:

Gener José Avilés Rodríguez

Ensenada, Baja California, August of 2022.

Universidad Autónoma de Baja California

Facultad de Ingeniería, Arquitectura y Diseño

Topological Data Analysis of Eye Fundus Digital Images

THESIS

presented to partially fulfill the needed requirements to obtain the degree of

DOCTOR IN SCIENCE

Presented by

Gener José Avilés Rodríiguez

Approved by:

Dr. Juan Iván Nieto Hipólito
Advisor

Dra. María de los Ángeles Cosío León
Co-Advisor

Dr. Gerardo Salvador Romo Cárdenas
Committee Member

Dr. Juan de Dios Sánchez López
Committee Member

Dr. Patricia Radilla Chávez
Committee Member

Ensenada, Baja California, August of 2022.

Summary of the thesis of **Gener José Avilés-Rodríguez**, presented to partially fulfill the needed requirements to obtain the degree of DOCTOR IN SCIENCE from the Maestría y Doctorado en Ciencias e Ingeniería (MYDCI) from UABC. Ensenada Baja California, México, August of 2022.

Topological Data Analysis of Eye Fundus Digital Images

Summary Approved by:

Dr. Juan Iván Nieto Hipólito
Thesis Advisor

In this work the use of Topological Data Analysis in digital fundoscopy is presented, specifically to achieve steps in the preprocessing stages such as background segmentation and Image Quality Assessment, towards the integration of systmes for Computer Aided Diagnosis. The method becomes relevant since it does not require a relatively high volume of images to achieve applicable results and does not require the use of high performing hardware. The approach is generated as a transdisciplinary effort between the areas of computational topology, digital image processing and clinical medicine. The process and the results fulfill the definition of translational research and set the basis to further explore medical images from a translational approach.

Keywords: *Digital Fundoscopy, Medical Images, Topological Data Analysis, Computational Topology, Image Quality Assessment.*

Dedication

To my daughter Mane Isabel, may you one day grasp the strength you have inspired in me to see this projet through, may it provide a context for you to flourish and enjoy the discipline of staying curious. It is you who has been the light at the end of the tunnel, when things did not go as planned, when I thought I was not going to be able to finish, you have been the source of fresh air and endless hope. May we be able to stay curious, critical, and knowledgable together. May you grant me the opportunity to go with you in your path of discovery until you choose to fly by yourself.

To my parents, this would not have been possible without your help in times when I could not carry myself. Life will not sufice me to pay back how generous and caring you have been with me. This path would have been very unlikely if I had not had the influence of both your academic lives. In a sense, this project is an extension of what you started in your lives and taught us by example.

Acknowledgments

To the members of the thesis committee who have accompanied me at different stages of this journey. *Dr. Juan Iván Nieto Hipólito*, for being a master in guiding by letting me do, for knowing when to intervene and when to point me towards a different horizon. I wish, one day, I may emulate your ability to guide by letting do. To *Dr. María de los Ángeles Cosío León*, I have appreciated your keen observations and straight to the point comments, I will allways be in debt with you for being willing to take a "blind shot" by starting a journey with a physician with a serious interest in data analytics. To *Dr. Gerardo Salvador Romo Cárdenas*, you have been like a brother to me, your guidedance has enabled me and facilitated new perspectives to specific problems within the research walk of this process as well as the process of becoming a researcher. To *Dr. Juan De Dios Sánchez López*, you kept a fresh perspective each time we met, it helped keep the project objective and balanced. To *Dr. Patricia Radilla Chávez*, for allowing me to imagine a way of continuing my doctoral work an move into a researcher and professor stage.

To my classmates and labmates, for their friendship, brotherhood and togetherness experienced while pursuing a high demanding degree.

To the MyDCI program in Facultad de Ingeniería, Arquitectura y Diseño from Universidad Autónoma de Baja California, for allowing a clinician to pursue trainning in the areas where his convictions, and the data, took him.

To the *Consejo Nacional de Ciencia y Tecnología* for the tuition and stipened support provided during my studies.

Contents

List of Figures

List of Tables

Chapter 1

Introduction

The coming of the era of big data, where information and communication technologies facilitate the generation of a significantly greater number of data available across many different disciplines, has also impacted the medical field. There is not a proportional amount of information derived from the growing pool of data available in the medical data [2]. The need for different approximations to data analytics in this field is very important.

One of the areas in which the phenomenon described in the previous paragraph is very tangible is with medical images. Digital images are processed as matrices of data where the 2D structure confines them particular characteristics for their analysis and interpretation.

Dimensionality reduction is one of the steps of the analytical process where areas of opportunity to facilitate further processes down the analytical pipeline can be explored.

1.1 Motivation

This project aims to contribute to the ongoing efforts to achieve feature selection and feature extraction of characteristics in digital fundoscopy images. The approach takes relevance given that the approximation is planned to keep mathematical and algorithmic phases as clinically significant as possible from the beginning, integrating tools from computational topology. This will enable the results to have clinical meaning and be usable by practitioners earlier in the analytical pipeline, which could turn into benefits for real patients with real pathologies sooner in the development process. As illustrated on Figure 1.1.

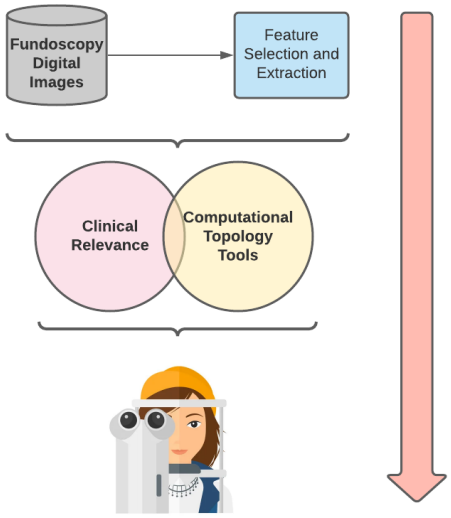

Figure 1.1: Visualization summarizing the justification for this work, where topological-based image analysis is kept clinically relevant.

1.2 Problem Statement

By the means of Topological Data Analysis (TDA), which is an approximation that precisely focuses on extracting general characteristics out of a large amount of data, we aim to maintain robustness despite of noisy and missing data, particularly for Image Quality Assessment (IQA). Through the interpretation of the topological characteristics obtained (topological groups). In contrast with expert-based approaches to IQA where high variability is typical and expected, Figure 1.2.

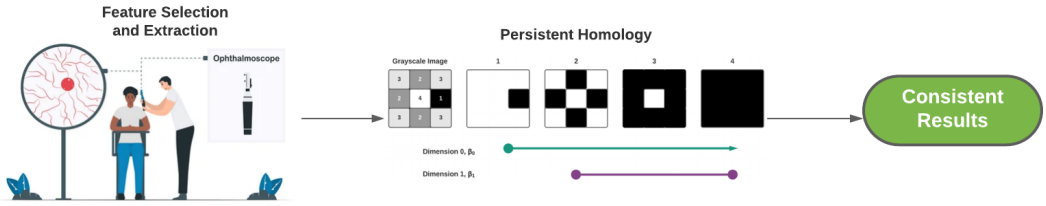

Figure 1.2: IQA based on TDA methods will tend to reduce variability in the results and help towards consistent results.

1.2.1 Research Questions

- What are the characteristics of digital fundoscopy images best analyzed by TDA and computational topology?
- How can the topological features of a digital fundoscopy image be translated into medical and biomedical information?
- Which are the characteristics of a Topological Data Analysis (TDA) pipeline for feature selection and extraction in digital fundoscopy images?

1.2.2 Hypothesis

The use of Topological Data Analysis in ophtalmological digital fundoscopy adds tools to the analytical pipeline providing clinically relevant results.

1.2.3 General Objective

To propose a methodology (approach) for the application of Topological Data Analysis in the process of feature detection and extraction in digital fundoscopy images. In order to find the most appropriate approach to obtain meaningful clinical results.

1.2.4 Specific Objectives

1. To identify the components of computational topology needed to perform TDA in biomedical images for feature extraction and selection.
2. To identify appropriate databases of eye fundus images for the implementation of TDA.
3. To develop a TDA pipeline to achieve feature detection and extraction in previously selected eye fundus images.
   (a) Integrate a preprocessing and quality evaluation approach.
   (b) Extract background and foreground in eye fundus images.
   (c) Image Quality Assessment.
4. To validate the results obtained by the TDA-based model against generally accepted techniques.

1.3 Structure of thesis

This work is divided into the following chapters:

Chapter 1 A brief introduction to the thesis project is given in this chapter, a justification for the approach taken is presented, as well as the problem statement and the sequence in content for the following chapters.

Chapter 2 Chapter 2 begins with a review of publich health implications for eye health, from economic to quality of life of the population affected. It then goes on to explore Digital Fundus Image Analysis, how it is defined, and methods used throught time. Then the concept of Topological Data Analysis (TDA) are introduced and essential concepts explored. This section finishes with the exploration of a TDA pipeline.

Chapter 3 In this chapter the method for interpreting digital images (image matrices) into mathematical objects in order to be analized by topological methods is presented. By the means of cubical complexes and luminescence-based persistence homology in the form of persistence diagrams. In order to feed these topological results to machine learning algorithms, methods for vectorization are presented as well. A brief review of performance metrics for classification algorithms in machine learning is incluede as well.

Chapter 4 This chapter shows and discusses the results obtained by applying the model presented in Chapter 3, it includes approaches that showed to be suboptimal and, eventually those that resulted useful towwards clinical use.

Chapter 5 Finally, conclusions are presented in this chapter, as well as future work and lines of research to be implemented as follow up.

Chapter 2

Review of the Literature

2.1 Computational Topology

2.1.1 Theory

This section aims to mention the generalities that spring from the theory of topology and computational topology. Figure 2.1 shows a visual summary of the general topics pertinent for this work. Section 2.4 goes into the details steming specifically from Topological Data Analysis (TDA) needed to approach the work summarized in this thesis.

In the process of assessing the state of the art in computational topology there were two topics that come up constantly in the literature review, Persistent Homology [3] and Network Topology [4]. Out of these two topics, persistent homology runs over into Topological Data Analysis, which is the current repository for the gathering of concepts and tools in the intersection of topology and discrete mathematics, *ergo* computational topology.

TDA, therefore, focuses on describing the shape of data understood as the "geometric properties of data which do not depend on the chosen coordinates, but rahter on intrinsic geometric properties of the objects" [5, 6]. As mentioned before, Section 2.4 will cover in more detail how this analytical paradigm is approached and how it can be used for the specific problem of this work.

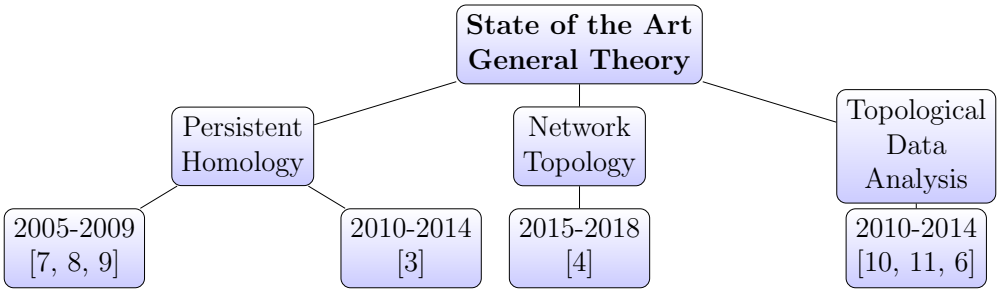

Figure 2.1: Diagram showing relevant areas related to general theory for the state of the art in this project.

2.1.2 Applications to Medicine and Biomedicine

A visual summary of the applications of TDA in medicine and biomedicine found in the literature up to the year 2021 is shown in Figure 2.2. The following paragraphs briefly discuss the results of the works found in the literature, with particular attention to applications in medical images.

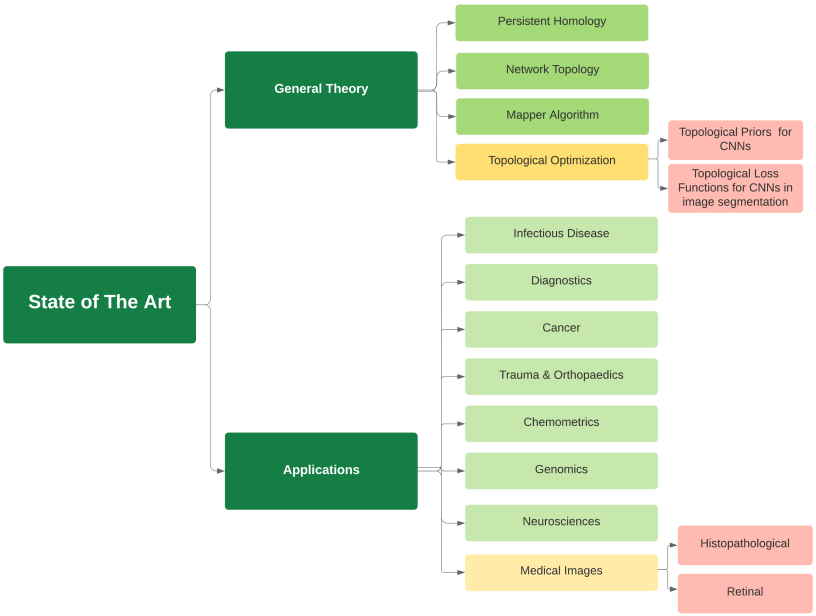

Figure 2.2: Summary of applications of Topological Data Analysis to Medicine and Biomedicine mentioned in the literature.

Neuroscience

Given that the brain is integrated as a rather large network of neurons and other supportive cell types, one of the areas in which TDA is being used is the approach to such networks to begin to understand them or make sense of them, as seen in the works by [12, 13] and [14]. Figures 2.3 and 2.4 show, respectively, the extraction of topological characteristics in $0-D$ and $1-D$ in the form of barcodes from hippocampal cell ensembles and the use of Rips complexes to describe the shape of point cloud data coming from signals gathered from the visual cortex.

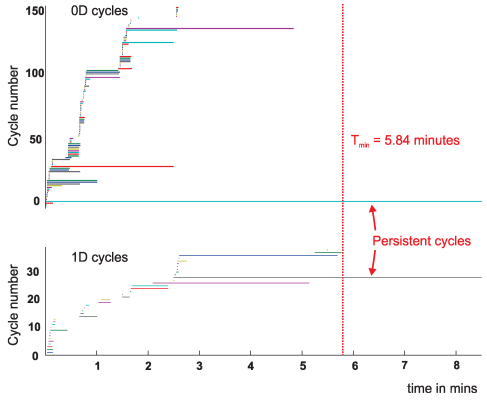

Figure 2.3: Barcodes shown $0-D$ and $1-D$ cycles persisting in an ensemble of hippocampal cells in charge of space maping in an animal model [13]

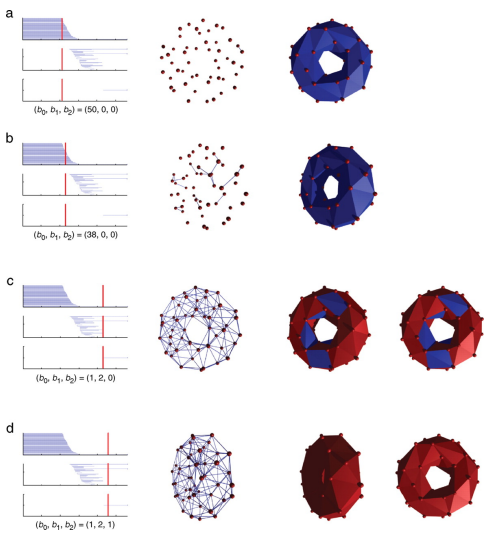

Figure 2.4: Construction of a Rips complex and barcodes generation in [12].

Another tool used in TDA is the Mapper algorithm [15], which, through an iterative

process proposes a representative graph of the data. An interesting use of this tool is the application to the discovery of precilincal spinal cord injuries and traumatic brain injuries in rat models by [16]. As shown on Figure 2.5, there are trends dettected that can be associated either to a traumatic brain injury or spinal cord injuries in rat models. One of the challenges with the use of mapper is that interpretations are very much dependent of the domain of the data, as well that the iterative nature of the algorithm translate into challenges for the reproducibility of results. Nevertheless, it is of use when approaching open problems which are still under study for their basic understanding. In these conditions, an iterative approach could be of help by sheding light into areas of possible correlation and/or causation.

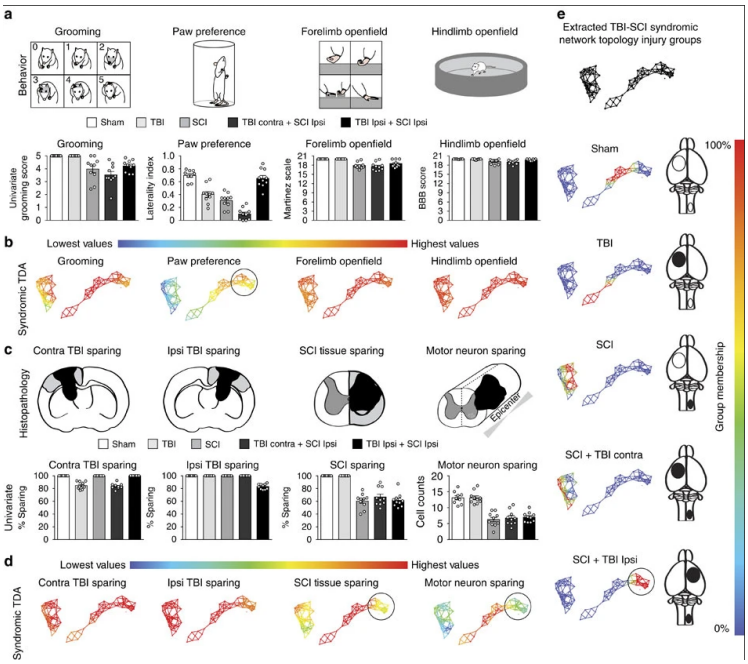

Figure 2.5: Mapper algorithm for brain injuries as applied by [16]. (a,b) Behavioral outcomes of forelimb function and (c,d) histopathology were mapped onto the topological network using TDA. Data from this model shows a distinct recovery pattern depending on whether the combined TBI (traumatic brain injury) is contralateral (contra) or ipsilateral (ipsi) to the SCI (spinal cord injury). (e) Each injury group occupies a distinct region of the network topology, highlighted as red nodes for 100% enrichment (heat map) for each particular injury model. Sham controls (n=9) and TBI-only (n=10) subjects are located in the right cluster. SCI-only (n=10) and SCI+TBI contra (n=10) are both located in the left cluster. SCI+TBI ipsi (n=10) interestingly are grouped next to the sham subjects in the right cluster (circled part of the network), due to a syndromic functional recovery similar to shams (a), despite showing no difference in pathology compared with subjects with SCI alone or SCI+TBI contra (c), [16].

Chemometrics

Chemometrics has multiple definitions, one of the accepted ones states: "Chemometrics is the chemical discipline that uses mathematical, statistical and other methods employing formal logic to design or select optimal measurement procedures and experiments, and to provide maximum relevant chemical information by analysing chemical data" [17, 18]. A typicall exmample of the use of TDA in this field is the construction of protein-protein interaction networks (PPI) based on differentially expressed proteins (DEPs), this produces a complex graph of interactions that then can be explored by the use of topological descriptors. On of the challenges in this approach is the attempt to achive dimensionality reduction of the descriptors by applying geometric tools, such as Principal Components Analysis (PCA), this makes explicability very challenging or impossible for the process. Nevertheless, this is a typicall example of the initial attempts to implement TDA in chemometrics, a filed that seems promesing for geometrical apporaches.

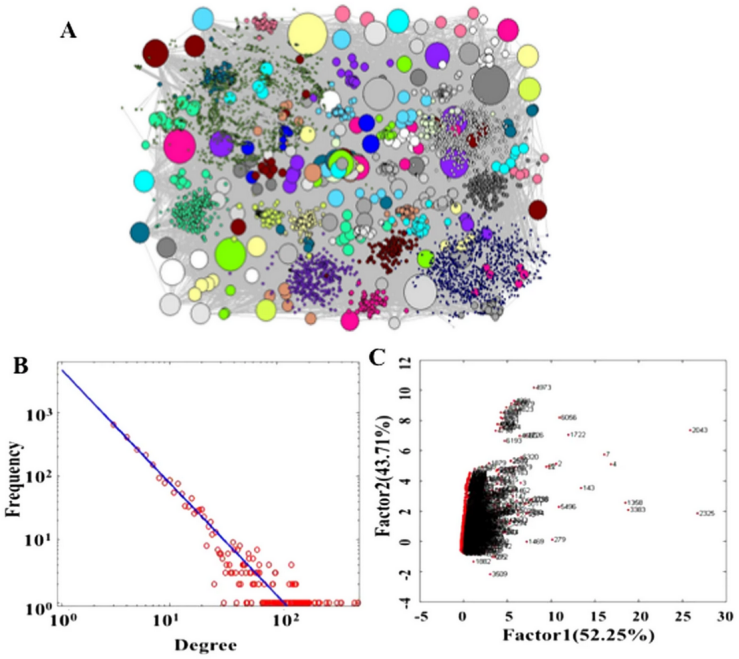

Figure 2.6: (A) The seeds of 244 DEPs were mapped onto a referenced database and were expanded to their first-degree neighbors, resulting in an extended network with 22 604 interactions between 6392 nodes. Different colors denote nodes with different degree and k-shell. (B) The degree distribution of the PPI network. (C) The contributions of the two factors in terms of factor scores f_1 versus f_2 are 52.25% and 43.71%, respectively, [19].

Genomics

The field of genomics is, by definition, an area of data in high volumes. Another characteristich that makes it suitable for the application of TDA is that the process of localizing specific association between gene loci or subsets of genes to concrete manifestations in the health-disease continum is very much an open problem. Therefore, topological approximations are attractive in order to add to the understanding of different open problems in the discipline. Figure 2.7 shows an implementation using TDA to enhance an analytical pipeline resulting on genomic associations.

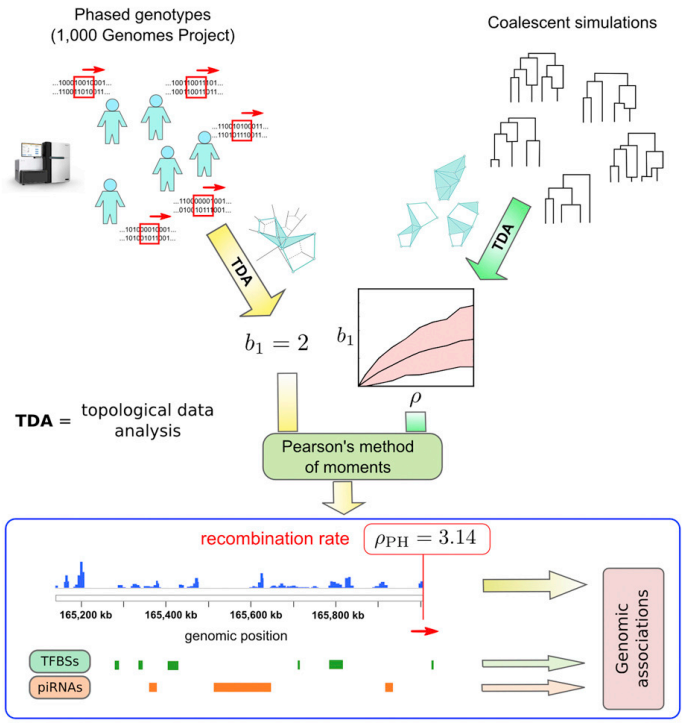

Figure 2.7: Summary of the use of TDA in genome wide maps of human recombination. In this approach TDA is able to capture recombination from large genomic samples, resulting into better results of high resolution recombination maps, and identification of binding sites [20].

Trauma & Orthopeadics

The finding of a publication [21] in the area of Traumatology and Orthopeadics using TDA was a surprise for the authors, this clinical field does not typically adopt analytical tools in early stages compared to other clinical specialties. Nevertheless, the use of the Mapper algorithm as an exploration for the prediction of cartilage lesions in knees of

patients with ostheoarthiritis (OA) was approached by taking into account the Kellgren-Lawrence (KL) grading for OA as well as sociodemographics and clinical data. The resulting graph and summary of analysis can be seen in Figure 2.8.

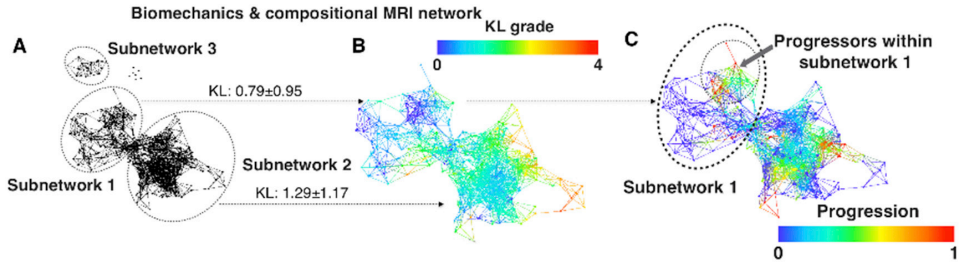

Figure 2.8: Figure showing (A) Network generated by Mapper, (B) same network colored by gender and KL grading, (C) shows detailes of the patients in the progression cohort, where a difference in the allocation of the graph can be appreciated for sever and less sever populations [21].

Cancer

The field of cancer research presents itself as a potentially good candidate for TDA, since it can intersect with genomics and chemometrics. Nevertheless, the study to link biomedical indicators with clincal outcomes remains an open problem. Following this perspective, [22] present a method based on the use of the Mapper algorithm to identify subgroups of breast cancer patients with particular mutational profiles linked to their survival. Figure 2.9 shows the resulting graph and associated subgroups linked to clinical outcomes. Again, in this case the approach to the problem was followed the use of the Mapper algorithm, with very limited ability for reproducibility. Nevertheless it is a preliminary approach that shows the power of TDA tools in the specific data domain.

Infectious Disease

Infectious diseases have also been approached with TDA tools, predominating the use of the Mapper algorithm as preliminary explorations of previously known indicators. In the case of Figure 2.10 an analysis of soil samples coming from four different geographical locations, all positive to E. Coli O157:H7, which is the strand responsible for food poisoning acompanied with hemorragic diarrhea and renal failure. It can become a public health issue quicly if not properly identified on time. Therefore the approach becomes relevant and pertinent, even if it is a preliminary result facing reproducibility challenges because of the iterative nature of the algorithm. Figure 2.10 shows the results reported by [23].

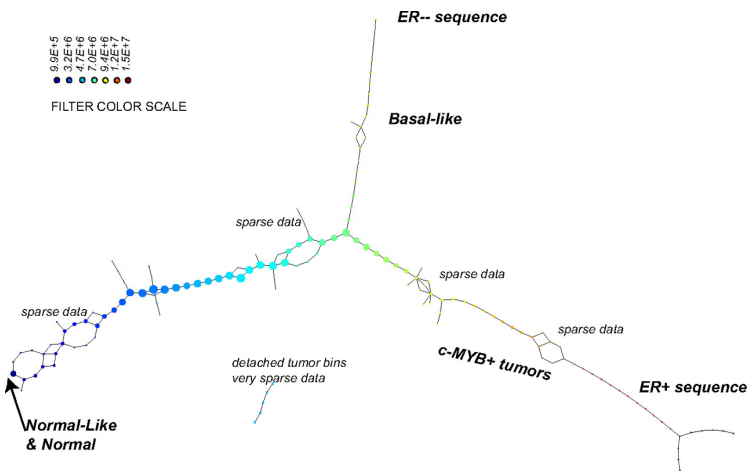

Figure 2.9: Analysis of breast cancer dataset showing three progression arms in the resulting graph generated by the Mappter algorithm, where each bin is colored by the mean of the filter map on the points. Showing tumors with different behaviours given the data, linked to clinical outcomes. Where ER^{-1} are mostly basal tumors, $c - MYB^{+}$ represents a subgroup not identified previously with agresive behaviour [22].

Medical Images – Ophtalmology

In this area there are approaches to include TDA in the process of classifying diabetic retinopathy [24], usgin the High-Resolution Fundus (HRF) Image Database [25], which contains images of high detail such as those obtained in an ophtalmic clinic or high end eye health center. Topological descriptors are extracted from these images and added to a dataset complemented with other image descriptors, then dimansionality reduction by feature selection was performed by using a Least Absolut Shrinkage and Selection Operator method (LASSO), the reduced dataset was then fed to a Support Vector Machine (SVM) to perform a classification of diabetic retinopathy presence or absence in eye fundus images. Figure 2.11 shows how a subsection of the image matrix was binarized by different threshold values to be interpreted as a mathematical object and calculate homology values in $\mathbb{R}^{1,2}$.

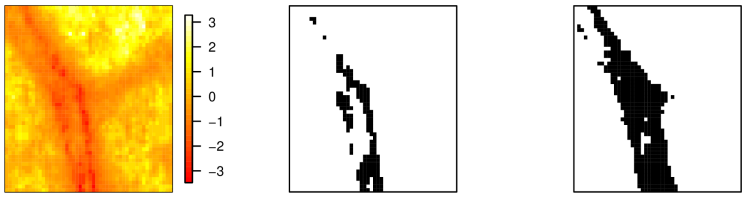

Figure 2.11: Example of a 50×50 image matrix sampled from grayscale eye fundus images on the left. With binarized images corresponding to $l = -1.5$ (center) and $l = -0.9$, notice that the luminsecence values are normalized from 8−bit digital images, [24].

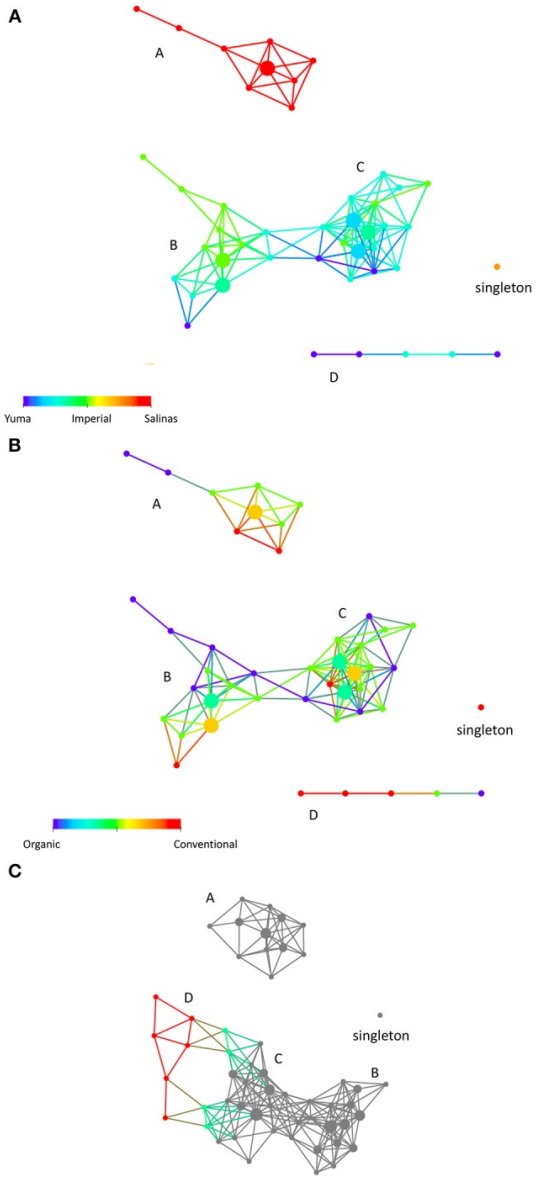

Figure 2.10: Topological network created by the Mapper algorithm using physical, chemical, and biological characteristics of soil samples. Four sub-networks can be identified (A-D) corresponding to the diferent geolocations where the samples were obtained [23].

Figure 2.12 presents a detail summary of the process followed by the authors to achive their results. Notice the use of topological descriptors, combined with summary statistics from digital images as a way to vectorize topological results in order to be fed in a way that is *understandable* for a machine learning algorithm.

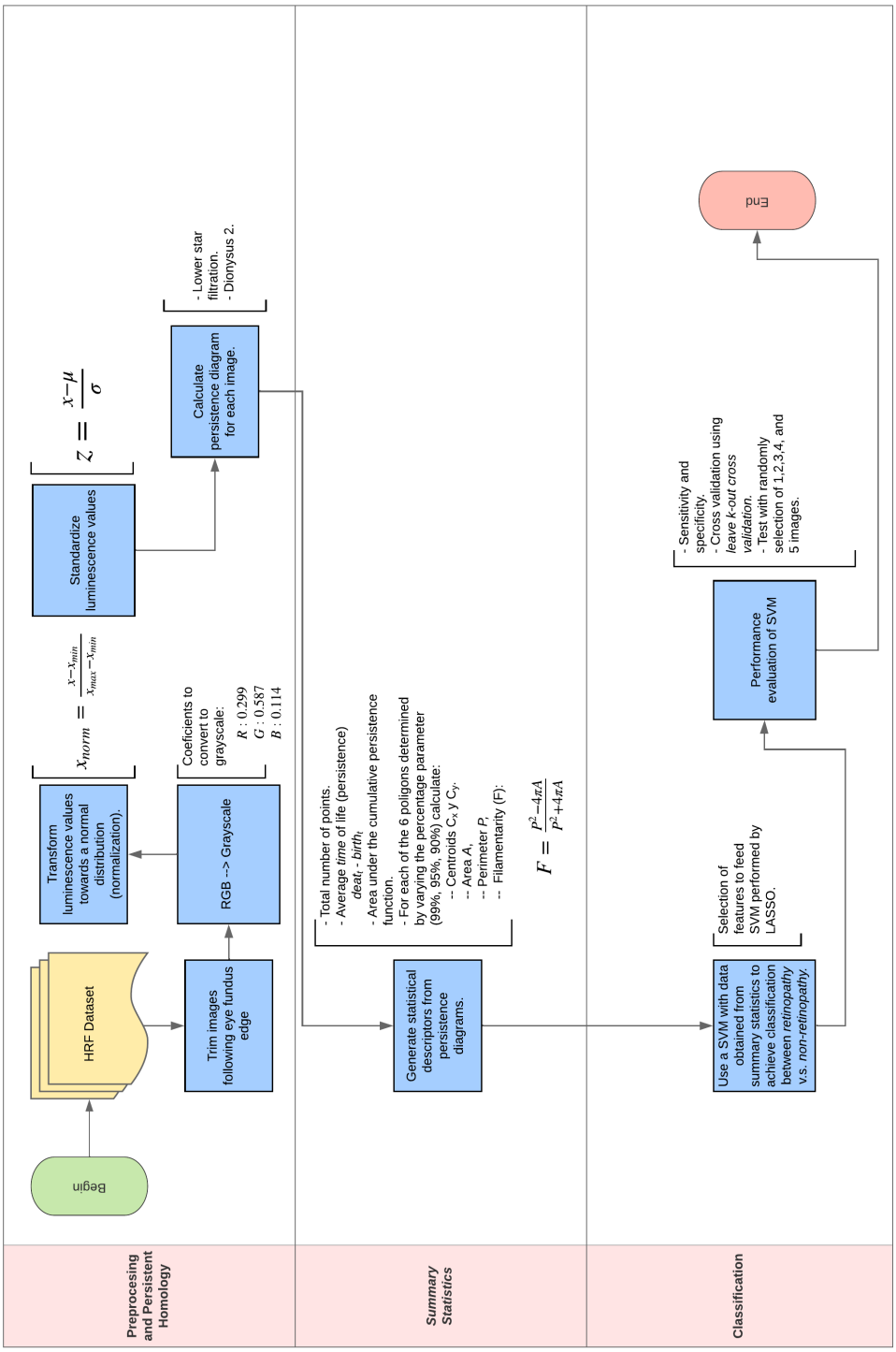

Figure 2.12: Detailed summary of the method followd in [24] to analyse high resolution eye fundus images for the identification of diabetic retinopathy. Using the High Resolution Fundus Image Database (HRF)

2.1.3 Medical Images: Digital Pathology

A very interesting series of publications highlighting the use of TDA in the field of digital pathology [26, 27, 28], specifically persistent homology of samples from Whole Slide Images (WSI) which are then binarized. They have moved into using topological informationa in combination with Convolutional Neural Networks (CNNs) to add robustness to the classification of the network. This specific work is summarized in detailed on Figure 2.14.

It is relevant to observe that, by using topological information it is possible to feed a CNN with either topological priors (a potential improve in trainning times) as well as explore topological loss functions for robust image segmentation of large images, in this case for digital pathology (histopathology) as highlighted on Figure 2.2.

Figure 2.13 shows part of the results achieved with the method proposed, where it is relevant the low proportion of false positives and negatives. The classification is performed at the pixel level, containning a granularity able to extract such metrics. From a medical perspective, these results come very close to how a pathologist would approach a report.

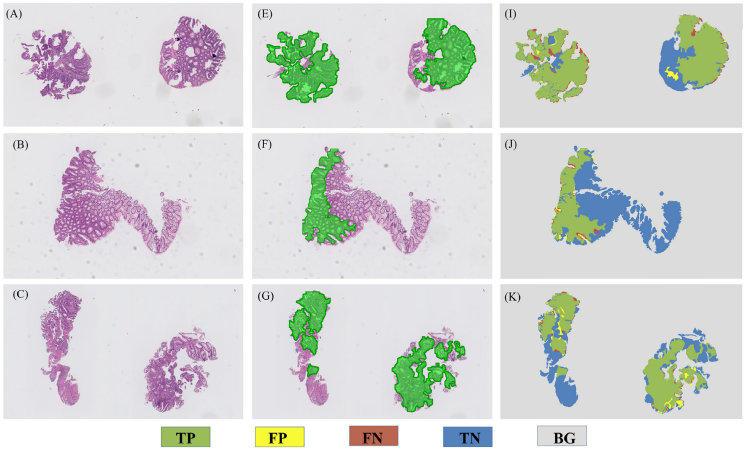

Figure 2.13: Results shown in [26] for fast tumor segmentation on selected WSI. (A)-(C) input WSIs, (E)-(G) predicted tumor regions, (I)-(J) results for true positives (TP), false positives (FP), false negatives (FN), and true negatives (TN) regions. Notice the low proportion of false negative pixels, which become very important in the clinical context of cancer.

2.1.4 The case for computational ophtalmology

Out of all the areas of applications of TDA in medicine and biomedicine, Ophtalmology is the one that was chosen to move forward with the project, there are two fundamental reasons for this decision:

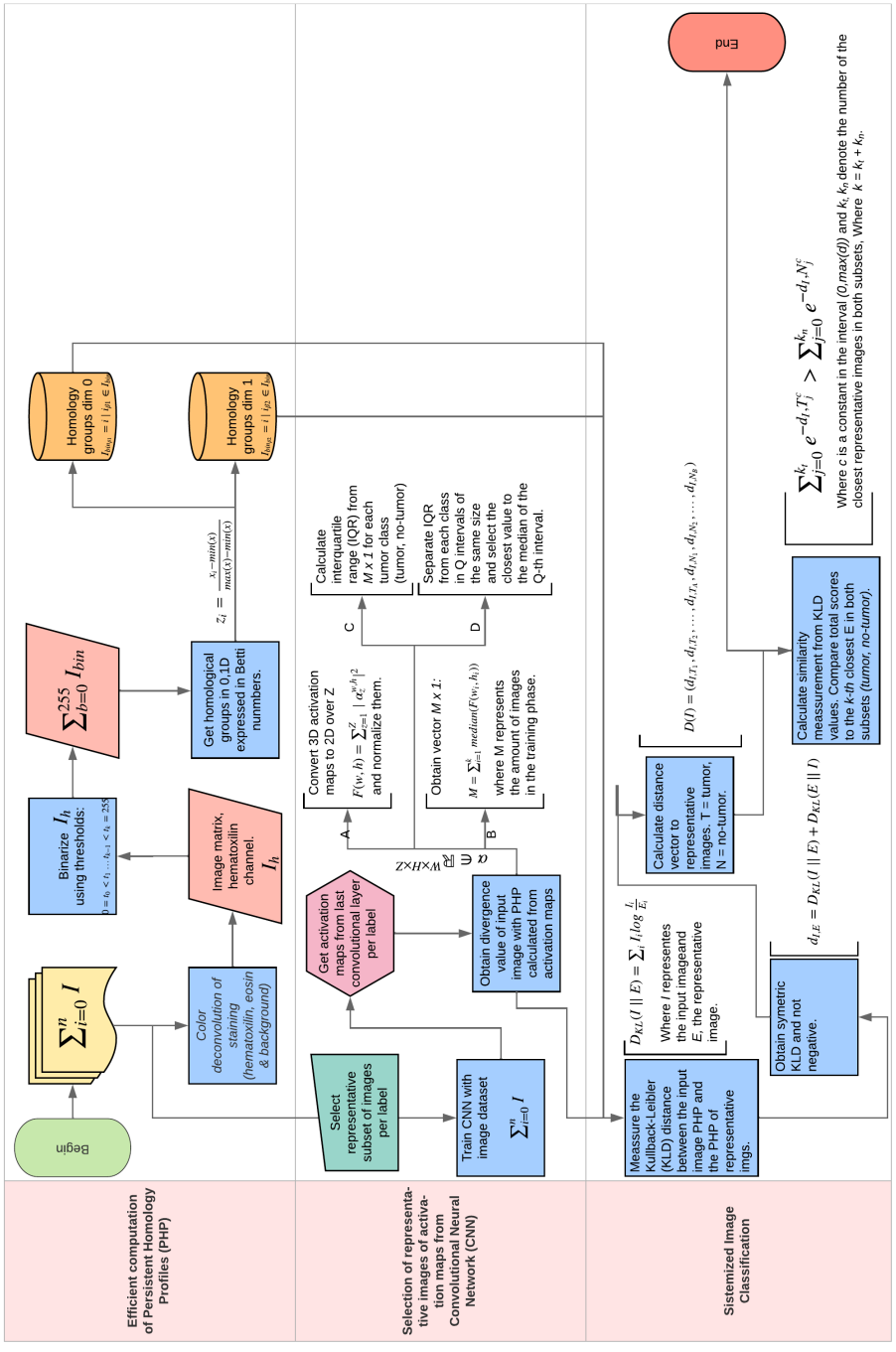

Figure 2.14: Qaiser and collaborators take a Whole Slide Image, section it in 250×250 at $20x$ zoom with microscope, these resulting images (*patches*) are called *images* in the algoritm [26].

- The public health value of the topic given the meassure of disease burden eye health pathologies represent in the world and, specifically, Mexico. Where the number one cause of non-reversible blindness is diabetic retinopathy. A more detailed and comprehensive argument on this area is presented on Section 2.2.

- The previous training on digital image processing available in the research group approaching this challenge (masters work on dimensionality reduction of medical images).

Therefore the case for the exploration of the use of computaional tools, specifically in topology, in the field of eye fundus imaging in the context of ophtalmological clinical approaches towards the construction and implementation of Computer Aided Diagnosis seems logical, pertinent and ethically percieved as a priority. Therefore the decision to pursue these issues in the context of computational ophtalmology [29].

2.2 Medical Dimension

2.2.1 Public Health

Eye health has a profoundly multidimensional effect in overall health, economics and social development for populations around the world [30]. Globally, there are more than 250 million people with vision impairment and over a billion with near-vision impairment. Globally, there are more than 250 million people with vision impairment and over a billion with near-vision im-pairment [31]. It is projected that over the next 30 years the amount of people affected by these issues will triple, reaching around 700 million, mostly due to the aging and growth of the population [31]. Even more, 90% of this loss occurs in low-income and middle-income countries leading to a substantial economic burden with a global annual estimate of over US$3 trillion [32].

Even though diagnostic and therapeutic strategies are available for the many causes of sight loss, for a significant amount of the global population at risk, they remain inaccessible mainly due to the lack of local eye care services and a considerable shortage and inefficient distribution of appropriately trained personnel [33]. In Mexico, according to [34], there are 3.56 ophtalmologist per 100 000 inhabitants, resulting in a constant deficit of accesibility to eye health professionals by a significant amount of the population in need of attention.

To address these challenges, with enough evidence and with potential to scale, these strategies can focus on capacity building of clinical personnel, and the use of technology to empower human resources [35]. Computational approaches in digital image analysis have been proposed as a strategy to strengthen and complement eye health teams, facili-tating accessibility to health services for medically underserved populations, one of the areas in which computational tools have proved to be useful is that of digital image processing as Computer Aided Diagnosis (CAD) systems [36].

2.2.2 Eye Fundus

A fundamental aspect in the evaluation of eye health is the assessment of eye fundus through ocular fundoscopy [37]. Figure 2.15 shows the anatomical landmarks a clinician looks for in a general evaluation of the eye fundus. This can be achieved by direct observation of the eye fundus through an ophthalmo-scope or through eye fundus images. As the methodology to evaluate a fundoscopy is not universal, it is strongly recommended that a systematic and organized approach be taken to this approach in the clinical practice [38]. This will allow the approach to be adapted and reproduced with a computational system that mimics the evaluations a clinician would perform during a regular consultation.

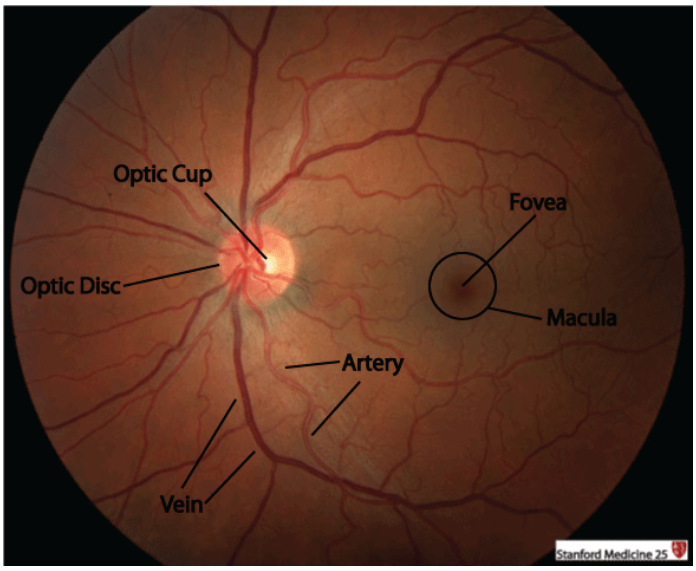

Figure 2.15: Anatomical landmarks evaluated in an eye fundus image assessment [39].

Nonetheless, state-of-the-art algorithms used for CAD systems in eye fundus images [40, 41, 42] tend to need large volumes of images in their training stages in order for them to achieve acceptable performance indicators, as well as accurately labeled images [43]. Therefore, the exploration of approaches to produce robust results with a relatively small-er volume of training images is important, given the current tendency in the field towards the use of deep learning approaches that require significantly large annotated datasets, which is a current challenge in medicine [44]. This will allow CAD tools to adjust to a clinical environment more rapidly, thus, facilitating expected outcomes.

2.3 Fundus Image Analysis

Fundus image analysis can be understood as the process of obtaining a digital image of the eye fundus and the analytical pipeline required to generate a CAD tool to support physicians in their clinical practice [45, 46]. Eye fundus imaging is the most established technique of retinal imaging, Figure 2.16 shows a summary of the components considered for this process.

As proposed by Abràmoff [45], Image Quality Assessment (IQA) is considered the first step in automated analysis techniques of eye fundus images. Development of IQA algorithms depends on the clinical application of the overall analysis [47, 48, 49] and can be classified in three general groups according to the techniques in which they achieve their objective:

1. Similarity based quality parameters.
    - These algorithms are based on parameters like clarity, focus, contrast, and illu-mination. They generally have low computational complexity and are preferred when using mobile or low powered devices, some examples can be seen in [50, 51] and [52]. Table 2.1 shows more detailed information on this approach.
2. Based on segmentation.
    - Techniques such as image structure clustering [53] or segmentation maps and feature analysis fall on this category [54]. Table 2.2 shows a more detailed information on this approach.
3. Deep learning.
    - The most recent approach in IQA, done with convolutional neural networks (CNNs) [40] and human-in-the-loop approaches combined with CNNs [55]. Table 2.3 shows a more detailed information on this approach.

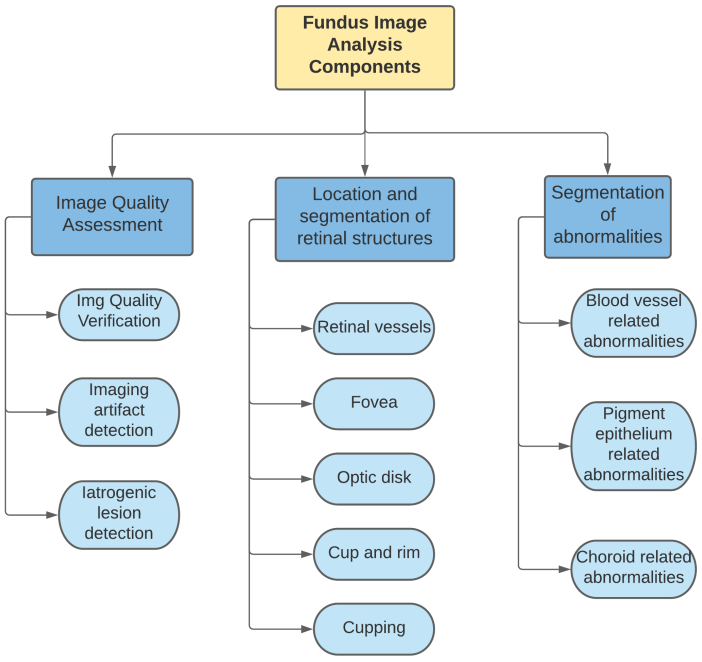

Figure 2.16: Fundus image analysis components as proposed by [45]

.

Work	Year	Quality parameter	Categories of quality	No. of images	Accuracy (%)	Pros	Cons
[51]	1999	intensity histogram	2	NS	NS	less complex; achieves high specificity as it measures similarity between characteristics of input image with good-quality fundus image	intensity histogram does not speak about the structural and local properties of the image
[47]	2001	edge magnitude and local intensity distribution	3	40	NS	contains analysis of structural properties; achieves high specificity	not robust to distortions like high compression and blur

Table 2.1: Similarity-based IQA algorithms for fundus images. Reproduced from [1].

[-1]Where: AUC = Area Under the Curve, and CA = Classification Accuracy.
[0]Matthews correlation coefficient: 0.864.

Work	Year	Quality parameter	Categories of quality	No. of images	Accuracy (%)	Pros	Cons
[56]	2003	blood vessel density	2	1746	SN: 95, SP: 84.3	matched filtering is easy and simple to implement, gives adequate performance in presence of Gaussian noise	effective only under pre-defined assumptions, not effective for smaller or larger size blood vessels
[49]	2006	blood vessel pixel count and field definition	2	1039	SN>99.1, SP: 89.4	emphasis given to the field definition and relative positioning of the structures present in the image	assumes fix parameters for the location of the structures hence not effective for cross data-set evaluation
[57]	2001	visibility of blood vessels and field definition	5	200	SN:100, SP: 93	effective performance for blur and Gaussian noise	sensitive towards different type of distortions like uneven illumination
[58]	2013	blood vessel pixel count	NA	58	SC: 0.89 with PSNR	due to patch-wise analysis this method is very effective in presence of uneven distortions additive Gaussian noise and Gaussian blur	method is tested over only two distortions, the naturalness property of images is low hence results obtained from SSIM and PSNR metrics may not be of much significance
[59]	2014	contrast blood vessels	2	47	89.36	effective for color and contrast distortions	effective only under pre-defined assumptions like size and shape

Table 2.2: Segmentation-based IQA algorithms for fundus images.

Work	Year	Method	Quality parameter	Categories of quality	Images	Accuracy (%)	Pros	Cons
[53]	2006	SVM	image structure clustering	2	2000	99.86	Features extracted are rotation and translation invariant	Less effective for the detection of color and blur distortions
[60]	2008	SVM	blood vessel density	2	84	SN: 100, SP: 92	Can effectively handle morphological changes in size blood vessels	Not effective for non-uniform distortions, tested over very small dataset
[61]	2010	SVM	Structural and generic features	2	301	95.3	Method combines both structural and generic properties, k-mean clustering is computationally faster	$k-$means clustering is sensitive to dataset any changes to the dataset will lead to completely different results
[62]	2012	SVM	field definition and blur	2	6696	96,95.5	Canny edge detection algorithm used for blood vessel segmentation is effective in presence of noise	Less efficient to assess the quality of fundus image in presence of Gaussian noise
[63]	2012	PLS	vessel density histogram, texture and sharpness	2	1884	96	Structural and generic properties are evaluated separately, included the subjective quality scores stationary wavelet	Method is not evaluated over the artefacts generated due to high compression
[64]	2013	SVM	symmetry of blood vessels	5	88	60	Transform used for the vessel segmentation is translation invariant	Evaluated over a very small dataset, not robust to color and blur artefacts
[65]	2014	SVM	contrast, blur and blood vessel density	2	370	95.8	In comparison to other methods this method quantifies the image quality on a fix scale	The performance of bottom hat filtering method used for the vessel segmentation relies upon the structuring element
[48]	2009	PLS	statistical features	2	2000	SN: 100, SP: 96	CIE L*a*b space model is effective for the extraction of color information	Not robust to distortions occurred due to compression and erroneous transmission
[50]	2014	ANN	color, focus, contrast and illumination	2	2032	99.87	Method analyses the focus, color, contrast, and illumination individually, tested over comparatively large dataset	Not robust to the artefacts generated due to high compression and erroneous transmission

Table 2.3 – *Continued from previous page*

Work	Year	Method	Quality parameter	Categories of quality	Images	Accuracy (%)	Pros	Cons
[66]	2014	FC	uneven illumination focus	2	1454	98	Method efficiently fuses the generic and structural properties, FC works efficiently with imprecise and incomplete data	MF used in FC works with "if and else" reasoning. However, it is not necessary that all the combined factors are equally important method is not efficient in presence of refractive errors
[67]	2016	SVM	uneven illumination and blur	2	3224	91.3	Due to block-wise analysis method is effective in presence of non-uniform distortions	Method is not efficient in presence of refractive errors
[68]	2016	DT and SVM	uneven illumination, color, blur and contrast	2	536	94.52	Dataset includes subjective evaluation, method works on HVS based feature extraction methods	Method is not evaluated over high compression and transmission error distortions
[69]	2017	DT,DL and SVM	llumination, naturalness property and structural information	2	4372	92.39	Gabor filters used for the optic disk segmentation are rotation, translation scale and illumination invariant	Classification accuracy is not up to the expected satisfactory level
[70]	2016	CNN	High-level features extracted from CNN	2	101	99.87	Simple network architecture	Evaluated over a very small dataset
[71]	2017	CNN	fusion of features extracted from CNN and saliency maps	2	5200	95.42	Unique feature extraction, evaluated over real distorted images significantly large dataset is used	No significant change in the performance of the system while not using the features extracted from saliency maps

Table 2.3: Machine learning-based IQA algorithms for fundus images.

2.4 Topological Data Analysis

2.4.1 Introductory Concepts

- **Topology** studies how space is connected.
  - This does not include how it communicates within itself (this is the domain of graph theory).
- **Algebraic topology** poses problems of connectivity as equivalent problems on algebraic objects (groups, fields, etc.), and maps between them (homomorphisms, homotopies, etc.).

In algebraic topology we cast problems on how space is connected a sequivalent problems on algebraic objects (groups, rings, etc), and maps between them (homomorphisms).

As a subfield of mathematics, algebraic topology started in the late 19th and early 20th century. Poincaré introduced the fundamental group first. Later Betti introduced homology groups, which are much easier to compute than the former [72].

Homology groups can be defined in many ways, one of them is using simplicial copmlexes. Simplicial homology is recomended for introductory approaches.

Topology mainly focuses in the analysis of characteristics preserved under continuous deformation in geometric objects [72] (for example noise or missing data represented in point clouds), in the last years there has been a significant rise in computational approaches to topological concepts for the analysis of data [73, 74, 5], this area is known as Topological Data Analysis (TDA). For the analysis of medical data TDA becomes an attractive tool given the robustness of the methods to missing and noisy data, which are common in this domain. In particular, for the case of images, they can be interpreted into mathematical objects called cubical simplicial complexes and then analyzed with topological methods to obtain characteristics to be used later in the analytical pipeline. In this work we focus in the interpretation of eye fundus images as cubical simplicial complexes and the obtention of homological groups (Betti numbers, $\beta_{(1,2)}$) to be used in the process of selecting optimal threshold values for binarizing a grayscale version of the image to obtain masks for background segmentation as well as Image Quality Evaluation through the vectorization of topological results for use with Machine Learning algorithms.

2.4.2 Fundamental Concepts in Topology

This secion contains definitions and fundamental concepts in the field of topology, which will help lay the foundation for later work.

Data domain representation

Definition 2.4.1 (Topology)**.** A topology on a set X can be mathematically defined as a subset $T \subseteq 2^x$ such that:

- If $S_1, S_2 \in T$, then $S_1 \cap S_2 \in T$.
- If $\{S_J | j \in J\} \subseteq T$, then $\cup_{j \in J} S_j$.
- $\emptyset, X \in T$.

Definition 2.4.2 (Topological Space)**.** A set $\mathbb{X}$ for which a topology T is defined therefore:

- $\emptyset \in T, \mathbb{X} \in T$
- $\forall S \subset T, \cup_{O \in S} O \in T$
- $(O_1 \in T, O_2 \in T) \Rightarrow (O_1 \cap O_2 \in T)$

Where:

- $T =$ topology.
- $O_i = i - th$ subcollection.
- $S =$ subset of subcollections.

Figure 2.17 shows an excercise with a set of three elements ($\mathbb{X}$) and 8 proposals of topologies ($\tau_{i_{\{1,2,\ldots,8\}}}$). Following Definition 2.4.1, some of these options are evaluated to see if they are indeed viable topologies for the given subset.

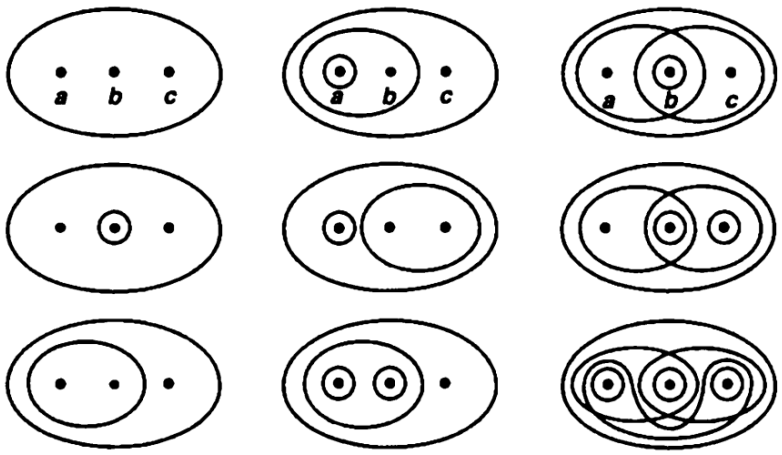

Figure 2.17: Example of a set of three elements with different topologies, as presented by James Munkres [72].

Figure 2.18 shows τ_1. Given:

- $\mathbb{X} = \{a, b, c\}$
- $\tau_1 = \{\{a\}, \{a, b\}, c\}$

Is τ_1 a topology on $\mathbb{X}$?

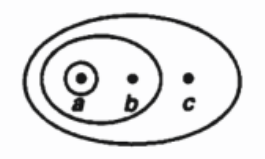

Figure 2.18: τ_1

Making sure Definition 2.4.1 is fulfilled:

- $\emptyset \in \tau_1$
- $a \in \tau_1, b \in \tau_1, c \in \tau_1 \therefore \mathbb{X} \in \tau_1$

$$\{a\} \cup \{a, b\} = \{a, b\} \in \tau_1 \quad \{a\} \cap \{a, b\} = \{a\} \in \tau_1$$
$$\{a\} \cup c = \{a\} \in \tau_1 \qquad \{a\} \cap c = \{\emptyset\} \in \tau_1$$
$$\{a, b\} \cup c = \{a, b\} \in \tau_1 \quad \{a, b\} \cap \{c\} = \{\emptyset\} \in \tau_1$$

$\therefore \tau_1$ is a topology in $\mathbb{X}$ and $(\mathbb{X}, \tau_1)$ is a valid topological space.

Figure 2.19 shows τ_8. Given:

- $\mathbb{X} = \{a, b, c\}$
- $\tau_8 = \{\{a, b\}, \{a, c\}, \{b, c\}, \{a\}, \{b\}, \{c\}\}$

Is τ_8 a topology on $\mathbb{X}$?

Figure 2.19: τ_8

Making sure Definition 2.4.1 is fulfilled:

- $\emptyset \in \tau_8$
- $a \in \tau_8, b \in \tau_8, c \in \tau_8 \therefore \mathbb{X} \in \tau_8$

$$
\begin{array}{ll}
\{a,b\} \cup \{a,c\} = \{a,b,c\} = \mathbb{X} \in \tau_8 & \{a,b\} \cap \{a,c\} = \{a\} \in \tau_8 \\
\{a,b\} \cup \{b,c\} = \{a,b,c\} = \mathbb{X} \in \tau_8 & \{a,b\} \cap \{b,c\} = \{b\} \in \tau_8 \\
\{a,c\} \cup \{b,c\} = \{a,b,c\} = \mathbb{X} \in \tau_8 & \{a,c\} \cap \{b,c\} = \{c\} \in \tau_8 \\
\{a\} \cup \{a,b\} = \{a,b\} \in \tau_8 & \{a\} \cap \{a,b\} = \{a\} \in \tau_8 \\
\{a\} \cup \{a,c\} = \{a,c\} \in \tau_8 & \{a\} \cap \{a,c\} = \{a\} \in \tau_8 \\
\{a\} \cup \{b,c\} = \{a,b,c\} = \mathbb{X} \in \tau_8 & \{a\} \cap \{b,c\} = \{\emptyset\} \in \tau_8 \\
\{b\} \cup \{a,b\} = \{a,b\} \in \tau_8 & \{b\} \cap \{a,b\} = \{b\} \in \tau_8 \\
\{b\} \cup \{a,c\} = \{a,b,c\} = \mathbb{X} \in \tau_8 & \{b\} \cap \{a,c\} = \{\emptyset\} \in \tau_8 \\
\{b\} \cup \{b,c\} = \{b,c\} \in \tau_8 & \{b\} \cap \{b,c\} = \{b\} \in \tau_8 \\
\{c\} \cup \{a,b\} = \{a,b,c\} = \mathbb{X} \in \tau_8 & \{c\} \cap \{a,b\} = \{\emptyset\} \in \tau_8 \\
\{c\} \cup \{a,c\} = \{a,c\} \in \tau_8 & \{c\} \cap \{a,c\} = \{c\} \in \tau_8 \\
\{c\} \cup \{b,c\} = \{b,c\} \in \tau_8 & \{c\} \cap \{b,c\} = \{c\} \in \tau_8 \\
\{a\} \cup \{b\} = \{a,b\} \in \tau_8 & \{a\} \cap \{b\} = \{\emptyset\} \in \tau_8 \\
\{a\} \cup \{c\} = \{a,c\} \in \tau_8 & \{a\} \cap \{c\} = \{\emptyset\} \in \tau_8 \\
\{b\} \cup \{a\} = \{a,b\} \in \tau_8 & \{b\} \cap \{a\} = \{\emptyset\} \in \tau_8 \\
\{b\} \cup \{c\} = \{b,c\} \in \tau_8 & \{b\} \cap \{c\} = \{\emptyset\} \in \tau_8 \\
\{c\} \cup \{a\} = \{a,c\} \in \tau_8 & \{c\} \cap \{a\} = \{\emptyset\} \in \tau_8 \\
\{c\} \cup \{b\} = \{b,c\} \in \tau_8 & \{c\} \cap \{b\} = \{\emptyset\} \in \tau_8
\end{array}
$$

$\therefore \tau_8$ is a topology on $\mathbb{X}$ and $(\mathbb{X}, \tau_8)$ is a valid topological space.

Figure 2.20: Not all collections of subsets are a topology on $\mathbb{X}$. The following examples are not.

Figure 2.20 shows two collections of sets with relationships that cannot be considered topoloiges on the sets. The following examples will walk through subsets of $\mathbb{X}$ that do not fulfill the definition for topology on the set.

Figure 2.21, given:

- $\mathbb{X} = \{a, b, c\}$
- $\tau_\alpha = \{\{a\}, \{b\}, c\}$

Is τ_α a topology on $\mathbb{X}$?

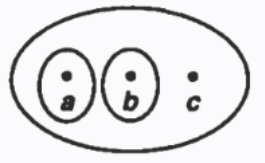

Figure 2.21: τ_α

Making sure Definition 2.4.1 is fulfilled:

- $\emptyset \in \tau_\alpha$
- $a \in \tau_\alpha, b \in \tau_\alpha, c \in \tau_\alpha \therefore \mathbb{X} \in \tau_\alpha$

$$\{a\} \cup \{b\} = \{a, b\} \notin \tau_\alpha \quad \{a\} \cap \{b\} = \{\emptyset\} \in \tau_\alpha$$
$$\{a\} \cup c = \{a\} \in \tau_\alpha \quad \{a\} \cap c = \{\emptyset\} \in \tau_\alpha$$
$$\{b\} \cup c = \{b\} \in \tau_\alpha \quad \{b\} \cap c = \{\emptyset\} \in \tau_\alpha$$

$\therefore \tau_\alpha$ **is not** a topology on $\mathbb{X}$ and $(\mathbb{X}, \tau_\alpha)$ **are not** a valid topological space.

Figure 2.22, given:

- $\mathbb{X} = \{a, b, c\}$
- $\tau_\beta = \{\{a, b\}, \{b, c\}\}$

Is τ_β a topology on $\mathbb{X}$?

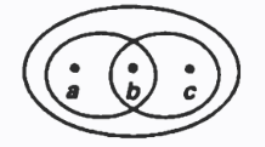

Figure 2.22: τ_β

Making sure Definition 2.4.1 is fulfilled:

- $\emptyset \in \tau_\beta$
- $a \in \tau_\beta, b \in \tau_\beta, c \in \tau_\beta \therefore \mathbb{X} \in \tau_\beta$

$$\{a, b\} \cup \{b, c\} = \{a, b, c\} = \mathbb{X} \in \tau_\beta \quad \{a, b\} \cap \{b, c\} = \{b\} \notin \tau_\beta$$

$\therefore \tau_\beta$ **is not** a topology on $\mathbb{X}$ and $(\mathbb{X}, \tau_\beta)$ **is not** a valid topological space.

Definition 2.4.3 (Opened Set)**.** A subset $\mathbb{A} \subseteq \mathbb{X}$ from a topological space $(\mathbb{X})$ is an *open* set of $\mathbb{X}$ if it belongs to T.

Open sets are topological spaces that do not contain their boundaries.

Definition 2.4.4 (Closed Set)**.** A subset $\mathbb{B} \subseteq \mathbb{X}$ from a topological space ($\mathbb{X}$) is *closed* if it´s complement ($\mathbb{X} - \mathbb{B}$) is *opened*.

Let $\mathbb{X}$ be a topological space $\{\mathbb{X}, \tau\}$. A subset A is *closed* if and only if it´s complement is an opened subset ($A \subset \mathbb{X} \iff A^c =$ conjunto abierto)

Class $\tau = \{\mathbb{X}, \emptyset, \{a\}, \{c, d\}, \{a, c, d\}, \{b, c, d, e\}\}$ defines a topology on $\mathbb{X} = \{a, b, c, d, e\}$.

Closed subsets of $\mathbb{X}$ are:

- $\emptyset$
- $\mathbb{X}$
- $\{b, c, d, e\}$
- $\{a, b, e\}$
- $\{b, e\}$
- $\{a\}$

Some observations:

- It is possible to have subsets that are closed and opened in the same topological space: $\{b, c, d, e\}, \{a\}$.
- It is possible to have subsets that are nither closed nor opened in the same topological space: $\{a, b\}, \{b, c, \}$.

Definition 2.4.5 (Interior)**.** The interior $\mathring{A}$ of a subset $A \subseteq \mathbb{X}$ is the union of all the sets contained in $\mathbb{A}$.

Definition 2.4.6 (Closure)**.** The closure $\bar{A}$ of a set $\mathbb{A} \subseteq \mathbb{X}$ is the intersection of all the closed sets containing $\mathbb{A}$

Formally, if $\{F_i : i \in I\}$ is the class of all closed subsets of $\mathbb{X}$ containing A, then:

$$\bar{A} = \cap_i F_i \tag{2.1}$$

As an excercise, we consider topology $\tau = \{\mathbb{X}, \emptyset, \{a\}, \{c, d\}, \{a, c, d\}, \{b, c, d, e\}\}$ in $\mathbb{X} = \{a, b, c, d, e\}$ with closed subsets from $\mathbb{X}$, which are:

$$\emptyset, \mathbb{X}, \{b, c, d, e\}, \{a, b, e\}, \{b, e\}, \{a\}$$

Then:

$$\{\bar{b}\} = \{a, b, c, d, e\} \cap \{b, c, d, e\} \cap \{a, b, e\} = \text{\{b,e\}}$$

$$\overline{\{a, c\}} = \{a, b, c, d, e\} = \mathbb{X}$$

$$\overline{\{b, d\}} = \{a, b, c, d, e\} \cap \{b, c, d, e\} = \text{\{b,c,d,e\}}$$

Definition 2.4.7 (Boundary)**.** A boundary in $\mathbb{A}$ is $\partial A = \bar{A} - \mathring{A}$.

In Figure 2.23, given subset A, the reader can visually appreciate the concepts of *closure* ($\bar{A}$), *interior* ($\mathring{A}$), and *boundary* (∂A). The illustration helps for an intuitive understanding of each of the definitions.

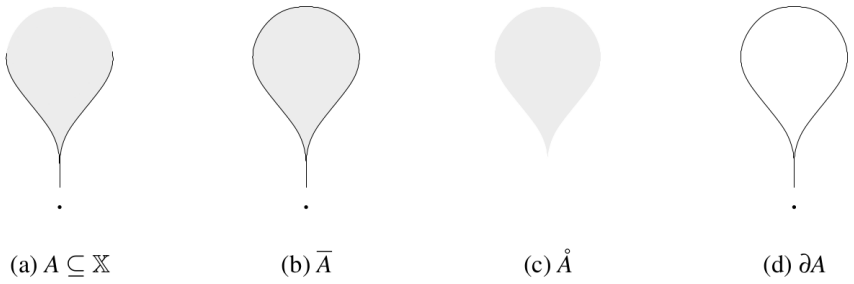

(a) $A \subseteq \mathbb{X}$ (b) $\overline{A}$ (c) $\mathring{A}$ (d) ∂A

Figure 2.23: *(a) Subset $\mathbb{A}$, (b) Closure of $\mathbb{A}$, (c) Interior of $\mathbb{A}$, (d) Boundary of $\mathbb{A}$.*

Definition 2.4.8 (Function)**.** A function $f : \mathbb{A} \to \mathbb{B}$ associates each of the elements of the topological space $\mathbb{A}$ to a unique element of the topological space $\mathbb{B}$.

Definition 2.4.9 (Injective Function)**.** A function $f : \mathbb{A} \to \mathbb{B}$ is injective if, for each pair $a_1, a_2 \in \mathbb{B}$ such that $a_1 \neq a_2, f(a_1) \neq f(a_2)$.

Figure 2.24 provides a visualization of an injective function.

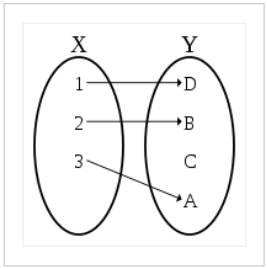

Figure 2.24: Injective function.

Definition 2.4.10 (Bijective Function)**.** A function $f : \mathbb{A} \to \mathbb{B}$ is bijective if, for each element $b \in \mathbb{B}$ there exists exactly one element in $a \in \mathbb{A}$ such that $f(a) = b$. It is said then that f is a *bijection* or *one-to-one*.

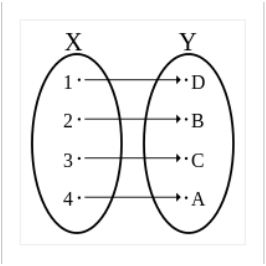

Figure 2.25: Bijective function.

Definition 2.4.11 (Continuous Function)**.** A function $f : \mathbb{A} \to \mathbb{B}$ is continuous if, for each open subset $\mathbb{C} \in \mathbb{B}$, set $f^{-1}(\mathbb{C})$ is an open subset of $\mathbb{A}$.

A classical definition of continuous functions in Eucledean spaces:

- Let $f : \mathbb{R}^n \to \mathbb{R}^m$.
- f is continuous at $\overline{x} \in \mathbb{R}^n$ if $\exists \delta > 0$ for every $\epsilon > 0$ such that $\|f(\overline{y}) - f(\overline{x})\| < \epsilon$ whenever $\|\overline{y} - \overline{x}\| < \delta$ for every $\overline{y} \in \mathbb{R}^n$.
- f is continuous (in all of $\mathbb{R}^n$) if it is so at every $\overline{x} \in \mathbb{R}^n$.

In this notation lower case letters with an overline are representing vectors $(\overline{x}, \overline{y}, \overline{\mu}, \overline{\alpha}, etc)$.

En equivalent definition based on neighborhoods can be understood as follows:

- A subset N of $\mathbb{R}^n$ is a *neighborhood* of $\overline{x} \in \mathbb{R}^n$ if for some $r > 0$, the closed ball $B(\overline{x}, r)$ centered at $\overline{x}$ is contained entirely within N. As shown in Figure 2.26

*Neighborhood N can be open or closed.

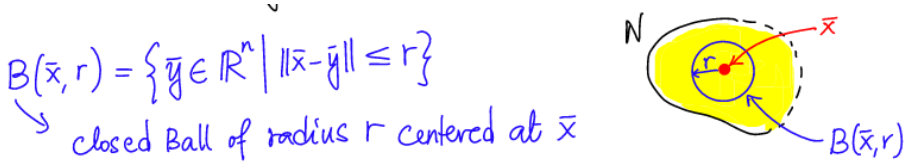

Figure 2.26: Visualization of definition of neighborhood.

- $f : \mathbb{R}^n \to \mathbb{R}^m$ is continuous if given any $\overline{x} \in \mathbb{R}^n$ and a neighborhood N of $f(\overline{x})$ in $\mathbb{R}^m$, $f^{-1}(N)$ is a neighborhood of $\overline{x}$ in $\mathbb{R}^n$.

Definition 2.4.12 (Homeomorphic Spaces)**.** Two topological spaces $\mathbb{A}$ and $\mathbb{B}$ are homeomorphic if and only if there exists a continuous bijection $f : \mathbb{A} \to \mathbb{B}$ with and invers continuous function $f^{-1} : \mathbb{B} \to \mathbb{A}$.

Definition 2.4.13 (Manifold)**.** A topological space $\mathbb{M}$ es a $d-manifold$ if each element $m \in \mathbb{M}$ has an open neighborhood $\mathbb{N}$ homeomorphic to an open euclidian $d-ball$.

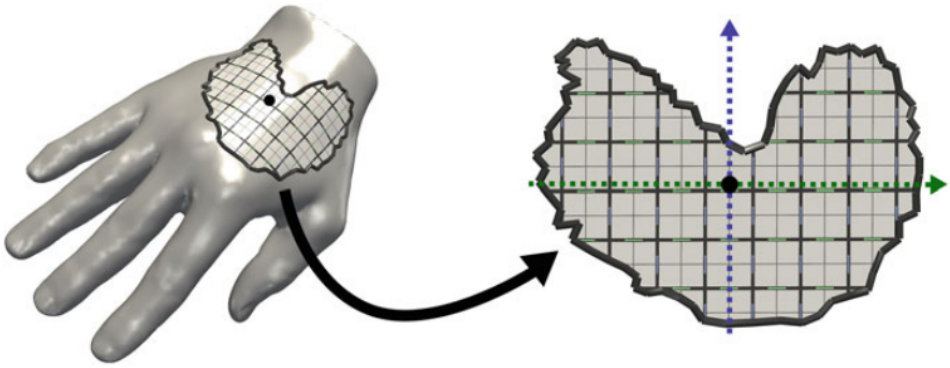

Figure 2.27: Example of a 2−manifold where any point on the surface has an open neighborhood (graph) which is homeomorphic to an open euclidean 2−ball, which can be unfolded to a plane.

Formalizing the Domain

Definition 2.4.14 (Convex set)**.** A subset $\mathbb{C}$ from an euclidean space $\mathbb{R}^n$ of $n-$dimention is convex if for each two points x and y from $\mathbb{C}$ and all $t \in [0,1]$, point $(1-t)x + ty$ also belongs to $\mathbb{C}$.

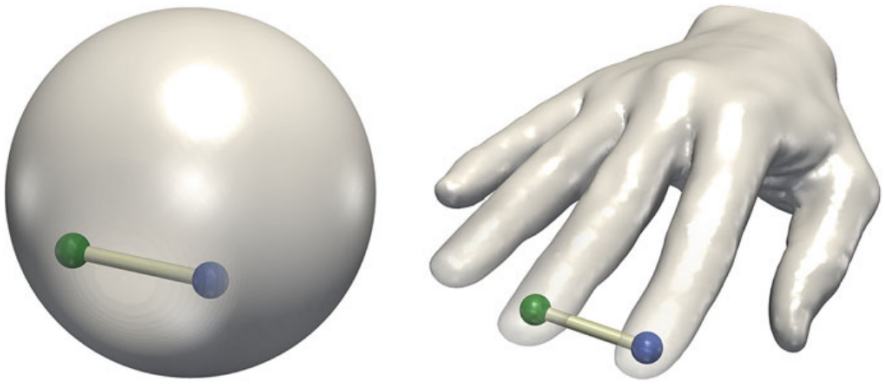

Figure 2.28: Example of a convex 3−manifold (left) and not convex (right). On the left, any two points (green and blue in this example) can be connected by a line segment contained in the volume. The previous is not true for the case on the right.

Definition 2.4.15 (Simplex)**.** A $d-$simplex is a convex hull σ of $d+1$ affine points independent from an euclidian space $\mathbb{R}^n$, with $0 \leq d \leq n$. Where d is the dimension of σ.

Definition 2.4.16 (Vertex)**.** A vertex v is a $0-$simplex in $\mathbb{R}^3$.

Definition 2.4.17 (Edge)**.** An edge e is a $1-$simplex in $\mathbb{R}^3$.

Definition 2.4.18 (Triangle)**.** A triangle t is a $2-$simplex in $\mathbb{R}^3$.

Definition 2.4.19 (Tetrahedron)**.** A tetragedrib T is a $3-$simplex in $\mathbb{R}^3$.

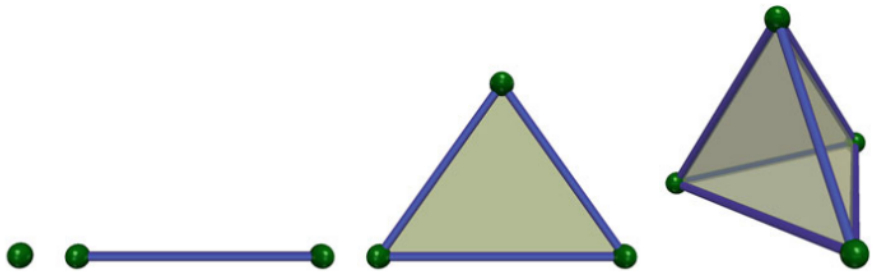

Figure 2.29: *Example of* $0, 1, 2, 3$*-simplices.*

Definition 2.4.20 (Face)**.** A face τ of a $d-$simplex σ is the simplex defined by a non-empty subset of $d+1$ points of σ, and it is written $\tau \leq \sigma$. Face τ_i is of $i-$dimension.

Therefore a $d-$simplex is the smallest combinatorial construction able to represent a $d-$dimentional neighborhood in euclidean space.

Definition 2.4.21 (Simplicial complex)**.** A simplicial complex $\mathscr{K}$ is a finite collection of non-empty simplices $\{\sigma_i\}$, such that each face τ from a simplex σ_i is also found in $\mathscr{K}$, and given two simplices σ_i and σ_j intersect on a common face or on none of them. Formalizing, a simplicial complex K is a collection of simplices such that:

- If $\sigma \in K$, then for each face $\sigma\prime$ of σ, we have $\sigma\prime \in K$.
- For two simplices $\sigma_1, \sigma_2 \in K, \sigma_1 \cap \sigma_2$ is $\emptyset$ or a face or both σ_1 and σ_2.

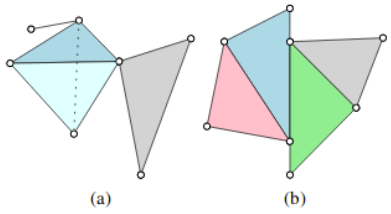

Figure 2.30: a) A simplicial complex. b) NOT a simplicial complex.

Exercises on construction of simplicial complexes:

- Indicate all the components from the simplicial complex K in Figure 2.31.

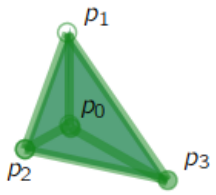

Figure 2.31: Simplicial complex K.

$$K = \begin{cases} \langle p_0, p_1, p_2, p_3 \rangle, \langle p_1, p_2, p_3 \rangle, \langle p_0, p_2, p_3 \rangle, \langle p_0, p_1, p_3 \rangle, \langle p_0, p_1, p_2 \rangle, \\ \langle p_0, p_1 \rangle, \langle p_0, p_2 \rangle, \langle p_0, p_3 \rangle, \langle p_1, p_2 \rangle, \langle p_1, p_3 \rangle, \langle p_2, p_3 \rangle, \langle p_0 \rangle, \langle p_1 \rangle, \langle p_2 \rangle, \langle p_3 \rangle \end{cases}$$

- Indicate all the components from simplicial complex Q on Figure 2.32.

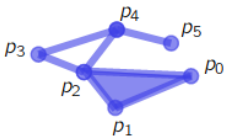

Figure 2.32: Simplicial complex Q.

$$Q = \begin{cases} \langle p_0, p_1, p_2 \rangle, \langle p_0, p_1 \rangle, \langle p_0, p_2 \rangle, \langle p_1, p_2 \rangle, \langle p_2, p_3 \rangle, \langle p_2, p_4 \rangle, \\ \langle p_3, p_4 \rangle, \langle p_4, p_5 \rangle, \langle p_0 \rangle, \langle p_1 \rangle, \langle p_2 \rangle, \langle p_3 \rangle, \langle p_4 \rangle, \langle p_5 \rangle \end{cases}$$

- Determine if J is a simplicial complex.

$$J = \{\langle a, b, c \rangle \langle a, b \rangle, \langle a, c \rangle \langle d, e \rangle\}$$

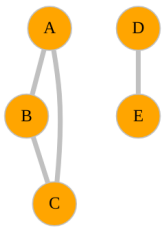

Figure 2.33: Graph J.

J **does not satisfy** the first requirement of Definition 2.4.21 for simplicial complexes, the following convertion $J \to K$ satisfies the requirements:

$$K = \{\langle a, b, c\rangle \langle a, b\rangle, \langle a, c\rangle \langle d, e\rangle\}, \langle a\rangle, \langle b\rangle, \langle c\rangle, \langle d\rangle, \langle e\rangle\}$$

Definition 2.4.22 ($p-$skeleton)**.** The $p-$skeleton is a simplicial complex K, denoted as $K^{(p)}$, is the subset of all the simplices in K of dimension p or less.

Taking simplicial complex K and using Figure 2.31 as a visual guide, the following $n-$skeletons are identified:

$$K^{(0)} = \{\langle p_0\rangle \langle p_1\rangle, \langle p_2\rangle, \langle p_3\rangle\}$$
$$K^{(1)} = \{\langle p_0, p_1\rangle \langle p_0, p_2\rangle, \langle p_0, p_3\rangle, \langle p_1, p_2\rangle, \langle p_1, p_3\rangle, \langle p_2, p_3\rangle, \langle p_0\rangle \langle p_1\rangle, \langle p_2\rangle, \langle p_3\rangle\}$$
$$K^{(2)} = \{\langle p_0, p_1, p_2\rangle, \langle p_0, p_1, p_3\rangle, \langle p_0, p_2, p_3\rangle, \langle p_1, p_2, p_3\rangle, \langle p_0, p_1\rangle, \langle p_0, p_2\rangle, \langle p_0, p_3\rangle, \langle p_1, p_2\rangle, \langle p_1, p_3\rangle,$$
$$\langle p_2, p_3\rangle, \langle p_0\rangle \langle p_1\rangle, \langle p_2\rangle, \langle p_3\rangle\}$$
$$K^{(3)} = K$$

In order to construct these concepts to describe a topological space, first we have to define what a neighborhood and a metric are. A topological space is obtained when there are points in the space that share a metric (sense of connectedness). To make this idea clearer, a definition of neighborhood must be established.

Definition 2.4.23 (Neighborhood)**.** A neighborhood of $x \in X$ is any $A \subseteq X$ such that $x \in \mathring{A}$.

Neighborhoods, which can be a topology, may be defined by the means of a metric. As shown in Figure 2.34.

Figure 2.34: a) A set $A \subseteq \mathbb{X}$. b) The closure $\overline{A}$ of set in a). c) Interior $\mathring{A}$ of set in a). d) Boundary of a set A which is equal to $\partial A = \overline{A} - \mathring{A}$, from [75].

Definition 2.4.24 (Metric)**.** A metric or ***distance function*** $d : X \times X \to \mathbb{R}$ is a function satisfying the following axioms:

1. For all $x, y \in X, d(x, y) \leq 0$, (**positivity**).
2. If $d(x, y) = 0$, then $x = y$, (**nondegeneracy**).
3. For all $x, y \in X, d(x, y) = d(y, x)$, (**symmetry**).
4. For all $x, y, z \in X, d(x, y) + d(y, z) \leq d(x, z)$, (**triangle inequality**).

Topological Space

We are given a set X and a non empty collection of subsets of X for each $\overline{x} \in X$ called the neighborhoods of $\overline{x}$. This is a topological space if it satisfies the following axioms:

1. $\overline{x}$ lies in each of its neighborhood.
2. Intersection of two neighborhoods of $\overline{x}$ is itself a neighborhood of $\overline{x}$.
3. If N is a neighborhood of $\overline{x}$, and $U \subseteq X$ contains N, then U is a neighborhood of $\overline{x}$.
4. If N is a neighborhood of $\overline{x}$, $\mathring{N}$, the *interior* of N is also a neighborhood of $\overline{x}$.

The interior of N is $\mathring{N} = \{\overline{y} \in N | N$ is a neighborhood of $\overline{y}\}$.

A topological space is obtained when there are points in the space that share a metric (sense of connectedness).

2.4.3 Key concepts on Simplicial Complexes

Building on Definition 2.4.21, dealing with the idea of a simplicial complex. The majority of concepts and theory in algebraic topology has been proposed for the continuous domain, which make it inaccesible to implement in a computer. One of the most used techniques to transfer these concepts to the discrete domain are **simplicial complexes**. An informal definition for simplicial complexes is that they are a combinatorial space that can represent a space. If this was to be applyed to surfaces, simplicial complexes are triangulations that allow a computer to represent a finite sample of a surface, Figure 2.35 shows a visual exmaple of simplices in different dimensions.

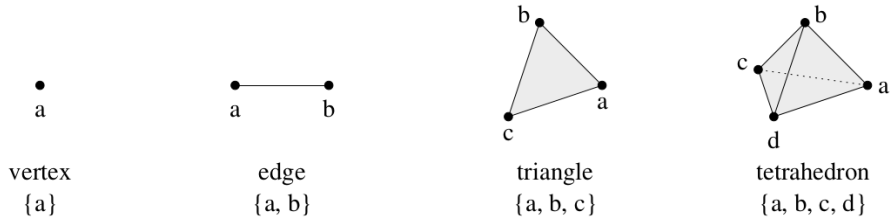

Figure 2.35: From left to right: a 1−simplex, 2−simplex, 3−simplex and 4−simplex, from [75].

A $k-$simplex is the convex hull of $k+1$ affinely independent points $S = \{v_0, v_1, \ldots, v_k\}$. The points in S are the vertices fo the simplex. For this definition we must clarify two basic concepts:

- A *convex hull* is a set which is a subset of an affine space where: for every pair of points within the region, every point on the straight line segment that joins the pair of points is also within the region, [76]. See Figure 2.36 for a visual representation.

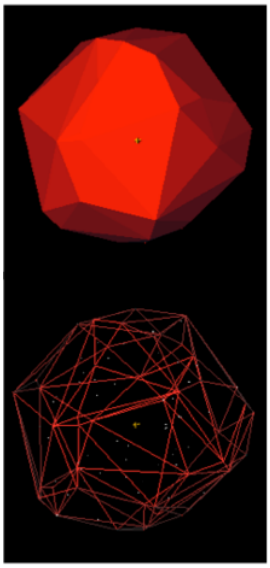

Figure 2.36: A 3D convex hull of a 120 point cloud, from [77].

Topological and geometrical characteristics are associated, generally, to continuous spaces. Data gathered as finite sets coming from observations do not reveal, directly, any type of topological information *per se*. A natural way of associating topological characteristics to discrete data is to *"connect"* those dots found close one to another, revealing, globally, a sense of the underlying continuous shape of the set [78].

Quantization of the notion of closeness between the point data is typically achieved using a meassure of distance (metric of dissimilarity). For Topological Data Analysis, it is frequently convenient to consider the sets of data as *discrete metric* spaces or *sampling of metric spaces* [78].

2.5 Topological Data Analysis Pipeline

2.5.1 Create connections between proximate points.

This stage is fulfilled by bulding a simplicial copmlex, for this there are many approximations. The following are commonly used ways of integrating a simplicial complex.

The Čech complex [79]

Given a set of points $P = \{p_1, p_2, \ldots, p_n\} \subset \mathbb{R}^d$ and a real value $r > 0$, a $k-simplex\langle\sigma = p_{i_0}, \ldots, p_{i_k}\rangle$ is in the Čech complex $C^r(P)$ if and only if:

$$\bigcup_{0 \leq j \leq k} \mathbb{B}(p_{i_j}, r) \neq \emptyset \tag{2.2}$$

The Vietoris-Rips complex [79]

Given a set of points $P = \{p_1, p_2, \ldots, p_n\} \subset \mathbb{R}^d$ and a real value $r > 0$, a $k-simplex\langle\sigma = p_{i_0}, \ldots, p_{i_k}\rangle$ is in the Vietoris-Rips (Rips) copmlex $R^r(P)$ if and only if:

$$\mathbb{B}(p_{i_j}, r) \cap \mathbb{B}(p_{i_{j\prime}}, r) \neq \emptyset \tag{2.3}$$

for any $j, j\prime \in [0, k]$.

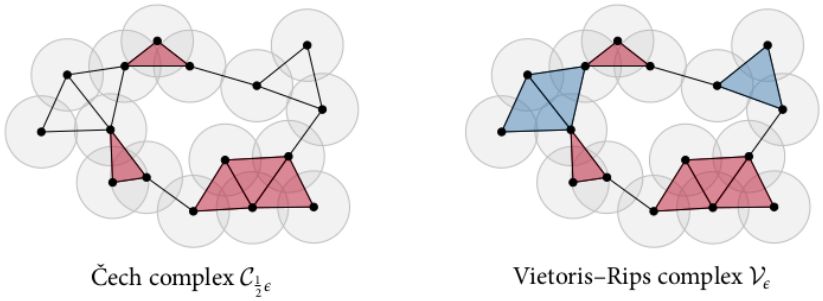

Figure 2.37: Visualization of the construction of a Čech and Vietoris-Rips complexes with ϵ as the parameter for constructing the ball around the point data. As shown by Bastian Rieck in [80].

Figure 2.37 shows the obtention of the Chech and Vietoris-Rips complexes of the same point cloud. Both complexes are visualized for the same value of the scale parameter (ϵ). The Čech complex contains a triangle for each subset of three balls with a non-empty intersection. By contrast, the Vietors-Rips complex contains a triangle whenever three balls have a pairwise intersection.

Delaunay complex [81]

Also called the Delaunay triangulation in lower dimensions.

Given a set of points $P = \{p_1, p_2, \ldots, p_n\} \subset \mathbb{R}^d$ and a real value $r > 0$, a $k-simplex\langle\sigma = p_{i_0}, \ldots, p_{i_k}\rangle$ is in the Delaunay complex $Del(P)$ if and only if there exists a ball $\mathbb{B}$ whose boundary contains vertices of σ and that the interior of $\mathbb{B}$ conatins no point from P.

A simplex in $Del(P)$ is also called a *Delaunay simplex*.

This approach is key in the fields of surface reconstruction and meshing. For points in high-dimensional space, the construction of a Delaunay complex is computationally expensive. Therefore, the Delaunay complex is less appealing for high dimensional data analysis.

Witness complex [82]

Witness complexes are used when one needs to build a complex on a subsample while leveraging information from the original points. Witness complexes can be defined as *weak* and *strong* as presented in the next paragraph. A simplex $\sigma = \langle q_0, \ldots, q_k \rangle$ is:

- ***Weakly witnessed*** by a point x if $d(q_i, x) \leq d(q, x)$ for any $i \in [0, k]$ and $q \in Q \setminus \{q_0, \ldots, q_k\}$.
- ***Strongly witnessed*** by a point x if in addition to being weakly witnessed by x, we also have that $d(q_i, x) = d(q_j, x)$ for any $i, j \in [0, k]$.

For a formal definition of a Witness complex we have to consider the following:

Given a set of points $P = \{p_1, \ldots, p_2\} \subset \mathbb{B}^d$ and a subset $Q \subseteq P$, the witness copmlex $W(Q, P)$ is the collection of simplices with vertices from Q whose all faces are weakly witnessed by some point in P.

2.5.2 Determine topological structure of complex.

In order to calculate homology groups, we must first define an orientation on the simplex by selecting a particular ordering of the set of vertices. An orientation on an $n-$simplex induces orientation on its $(n-1)-$faces.

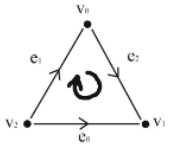

Figure 2.38: Orientation of a 2−simplex.

Figure 2.38 visually exemplifies the concept of the orientation of an $n-$simplex, using the example in $\mathbb{R}^2$. The following considerations can be derived from it:

- Given the orientation (v_0, v_1, v_2), the orientation induced on its 1-faces is $e_2 = (v_0, v_1)$, $e_0 = (v_1, v_2)$, $e_1 = (v_2, v_0)$.
- Formally:

- If $A^n = (v_0, v_1, \ldots, v_n)$ is an oriented *n-*simplex, then the orientation fo the (*n*-1)-face of A^n with vertex set $\{v_0, \ldots, v_{i+1}, \ldots, v_n\}$ is given by: $F_i = (-1)^i(v_0, \ldots, v_{i+1}, \ldots, v_n)$.

Chapter 3

Development of Research Strategy

Eye fundus images used for this project were taken from the EyePACS [83], MESSIDOR [84] and APTOS [85] projects. For the particular task of Image Quality Assessment we used labels proposed in [86], as pre-sented by [87]. We modeled the phenomenon as a binary classification between images with quality (good) and those without quality (bad), also adjusted for class imbalance by randomly selecting subsets by label of 2000 images each. Figure 3.1 shows a sample of images by label.

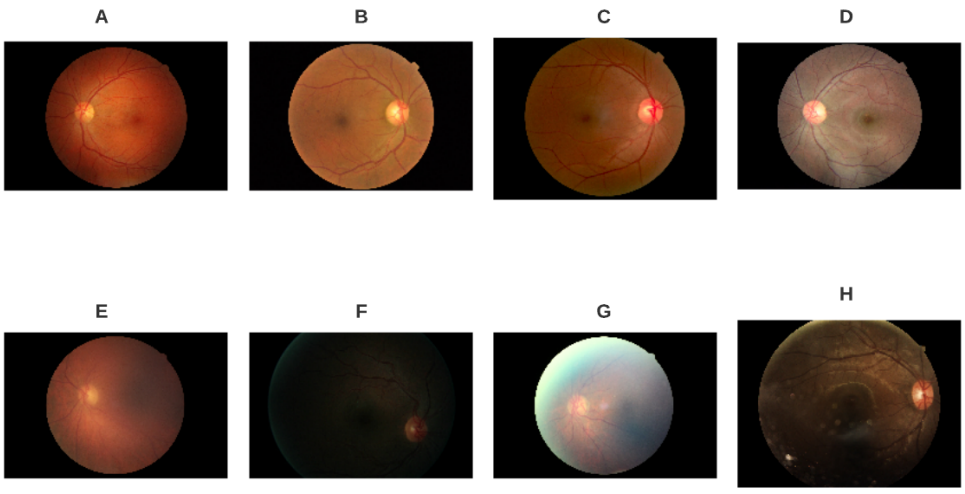

Figure 3.1: Examples of EyePACS images selected for the study with label good quality (A,B,C,D) and bad quality (E,F,G,H). Where there is variability within labels given by color, illumination, blurring, and anatomical landmarks.

3.1 Topological Interpretation of Digital Images

3.1.1 Cubical Complexes for the Representation of Digital Medical Images

Considering the need to use mathematical objects to represent 2D digital images, cubical complexes arise as a natural representation for this domain [88] given that pixels can be represented by 2-cubes and voxels by 3-cubes, as shown in Figure 3.2. This approach has already been used by [89] to analyze images of blood vessels by interpreting segmented images from Magnetic Resonance Imaging as cubical simplexes and calculating their homological groups.

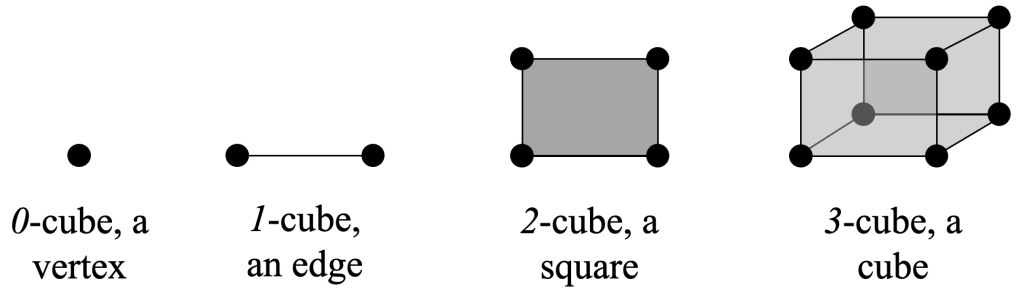

Figure 3.2: Examples of $n-$cubes

A cubical complex is a combinatorial structure used in topological analysis where a 0-cube is called a vertex, a $1-$cube, an edge, a $2-$cube a square, and a $3-$cube, a cube. This concept is built on the theory of elementary intervals and cubes as mentioned by [90].

In a cubical complex (K), multidimensional cubes (σ^d) play the role of simplices, where a finite cubical complex in $\mathbb{R}^d$ is a union of cubes aligned on the grid $\mathbb{Z}^d$ satisfying specific conditions as with simplicial complexes. A $d-$dimensional digital image can be considered as a discrete map $\mathcal{J} : I \subseteq \mathbb{Z}^d \to \mathbb{R}$. In this context an element $\sqsubseteq \in I$ is called a pixel when $d = 2$ and a voxel when $d = 3$. $\mathcal{I}(\sqsubseteq)$ is the correspondent intensity or grayscale value. For the case of a binary image, the discrete map is $\mathcal{B} : I \subseteq \mathbb{Z}^d \to \{0, 1\}$. We choose to represent images as cubical complexes where a pixel is represented by a $d-$cube and all its faces (adjacent lower-dimensional cubes) are added. A function on the resulting cubical complex $\mathcal{K}$ by extending the values of the pixels to all the cubes σ in $\mathcal{K}$ as Equation 3.1 shows.

$$\mathcal{J}'(\sigma) \coloneqq \min_{\sigma \text{ face of } \tau} \mathcal{J}(\tau) \tag{3.1}$$

3.2 Testing Persistent Homology in Normal and Pathological Eye Fundus Images

To be able to run a persistent homology analysis, a sense of a filtration is achieved by binarizing the grayscale image at each luminescence value as threshold, this results in a set of 256 binarized images [26], which can then be interpreted as cubical simplices and, therefore, obtain their homological groups in 1 and 2 dimensions expressed in Betti numbers (β_0, β_1). This process is summarized on Figure 3.3.

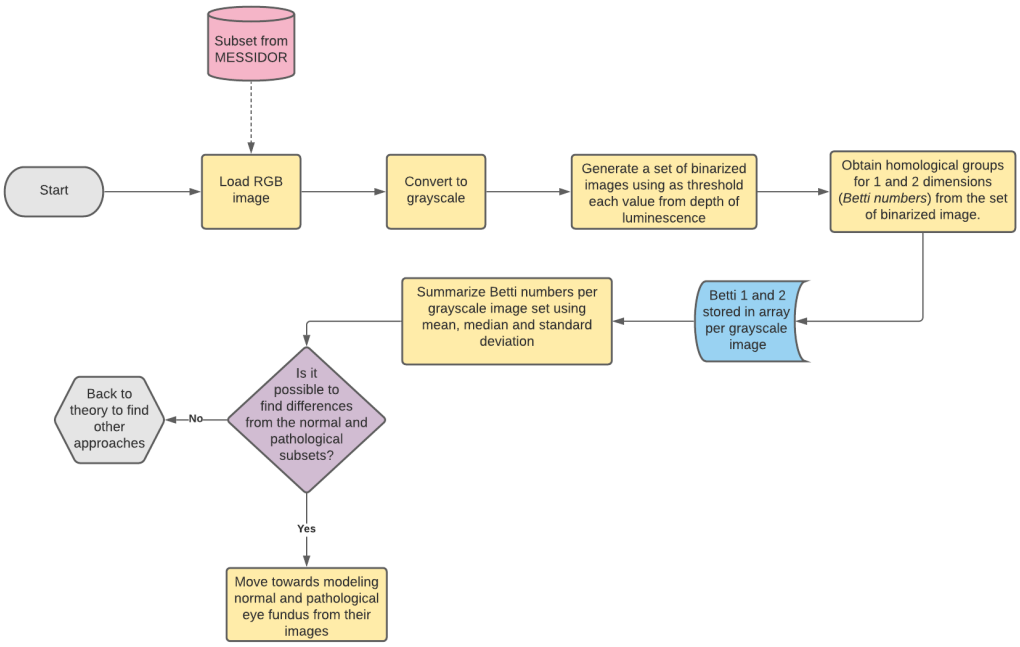

Figure 3.3: Flowchart of process described in this section.

Running this process **did not** show significant differences in the curves obtained from normal *versus* pathological images when summarized by the mean, median, and standard deviation of their values, and considering them as probability distributions for their comparison (See Table 3.1).

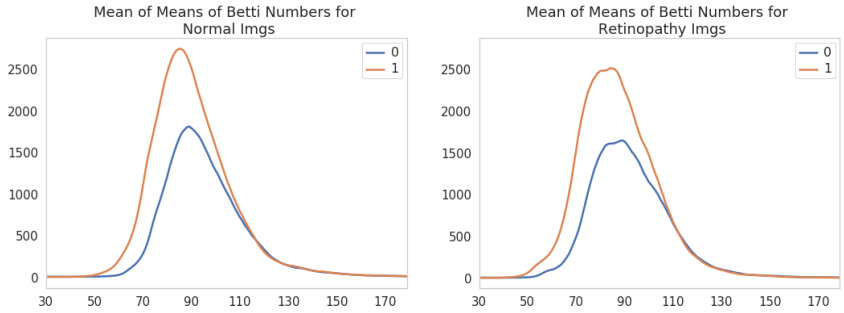

Figure 3.4: Means of Medians of *Betti* numbers values in 1 and 2 dimensions. The X axis has been cropped to luminescence values from 30 to 180.

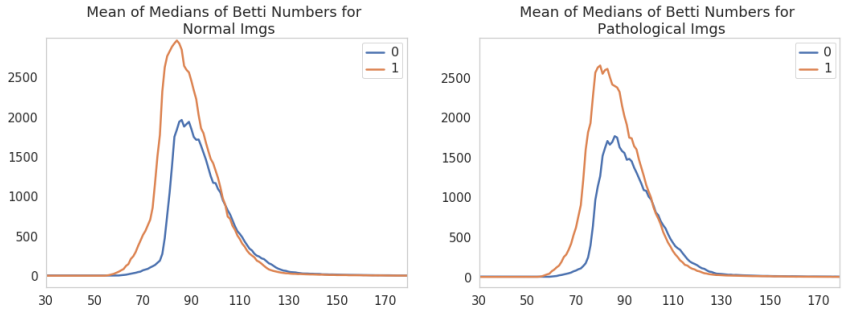

Figure 3.5: Means of Medians of *Betti* numbers values in 1 and 2 dimensions. The X axis has been cropped to luminescence values from 30 to 180.

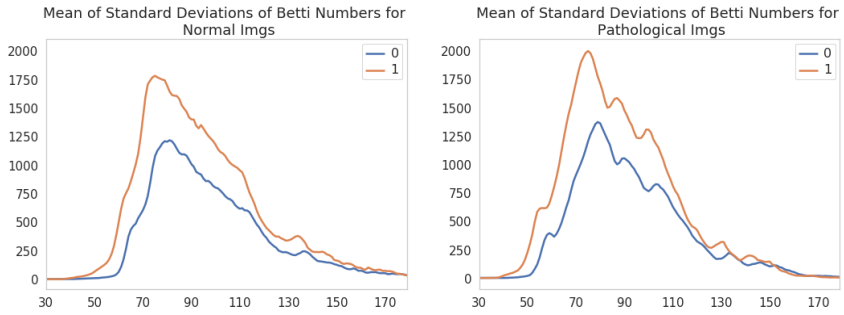

Figure 3.6: Mean of Standard Deviations of *Betti* numbers values in 1 and 2 dimensions. The X axis has been cropped to luminescence values from 30 to 180.

	p-value	
	β_0	β_1
$\overline{X}$ **of Means**	0.983	0.979
$\overline{X}$ **of Medians**	1	1
$\overline{X}$ **of Standard Deviations**	0.415	0.364

Table 3.1: Results of running Unpaired T-Test to the resulting vectors shown in Figures 3.4, 3.5 and Mann Whitney test to the resulting vector in Figure 3.6, comparing normal and pathological images.

Given that the results showed in Table 3.1 **do not** provide evidence to suggest significant differences between normal and pathological images, a more sensitive approach would seem to fit at this point to solidify the idea of a lack of significant difference or argue towards the need for a more granular method. This situation was approached by implementing an analysis with **cross correlation**.

3.3 Cross correlation, towards a more granular analysis

Cross-correlation is a technique measuring similarity in a pair of waveforms as a function of a time-lag applied to one of them. It is also known as a sliding dot product [91]. For continuous functions f and g, their cross correlation is defined as:

$$(f \star g)(\tau) \triangleq \int_{-\infty}^{\infty} \overline{f(t-\tau)} g(t) dt \tag{3.2}$$

Which is equivalent to:

$$(f \star g)(\tau) \triangleq \int_{-\infty}^{\infty} \overline{f(t-\tau)} g(t) dt \tag{3.3}$$

Where $\overline{f(t)}$ denotes the **complex conjugate** of $f(t)$, and τ is the displacement, also known as *lag* (a feature in f at t occurs in g at $t + \tau$)

This approach is used to measure similarity of one waveform to another. In this particular case we use it to extract granular differences in the waves that could be related to the health-disease continuum of retinal images, in the context of diabetic retinopathy.

The signals used are taken from Figure 3.4. A cross correlation analysis is performed using the mean of means as the statistical descriptor extracted from normal and pathological images. Luminescence values are used as the *lag* factor τ in Formula 3.2.

The results for Betti numbers in one and two dimensions can be seen in Figure 3.7, where it is evident that both, Betti 0 and 1, peak at very close τ values.

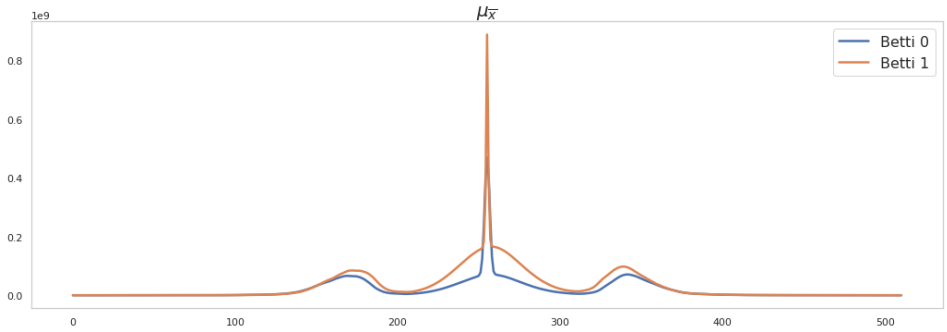

Figure 3.7: Cross correlation of mean of means, medians, and standard deviations of β_0 and β_1 numbers of normal and pathological images. A window at the same interval in the three images with potential relevant has been highlighted.

To test for difference in the waveform of correlations of the statistical descriptor obtained from normal and pathological images, a subtraction of waveforms following Formulas 3.4 and 3.5 is calculated for β_0 and β_1. We direct the reader to note that this process averages the difference of each of the images in the subset of normal and pathological, therefore allowing to compare the resulting waveform as the mean of the whole subset in question.

$$\overline{X}\left\{\left(\mu_{\overline{x}_{normal}} \star \sum_{i=1}^{n} normal_i\right) - \left(\mu_{\overline{x}_{patho}} \star \sum_{i=1}^{n} normal_i\right)\right\} \tag{3.4}$$

$$\overline{X}\left\{\left(\mu_{\overline{x}_{normal}} \star \sum_{i=1}^{n} patho_i\right) - \left(\mu_{\overline{x}_{patho}} \star \sum_{i=1}^{n} patho_i\right)\right\} \tag{3.5}$$

The resulting wave forms of this analysis can be seen in Figure 3.8. A Wilcoxon test was performed to evaluate for dissimilarity of the wave forms from the subset of 20 units of luminescence shown in the same Figure. Table 3.2 shows the results, where the statistically significant difference between normal and pathological is evident at, both, β_0 and β_1 values.

	p-value
β_0	0.0111
β_1	0.0003

Table 3.2: Results of running a Wilcoxon test to the regions of interest of wave forms in Figure 3.8, with a 95% confidence interval.

Results reported in Table 3.2 give evidence of a **statistically significant difference** between the wave form from normal *versus* pathological images. This allows for the argument that extracting homological groups in 1 and 2 dimensions from cubical

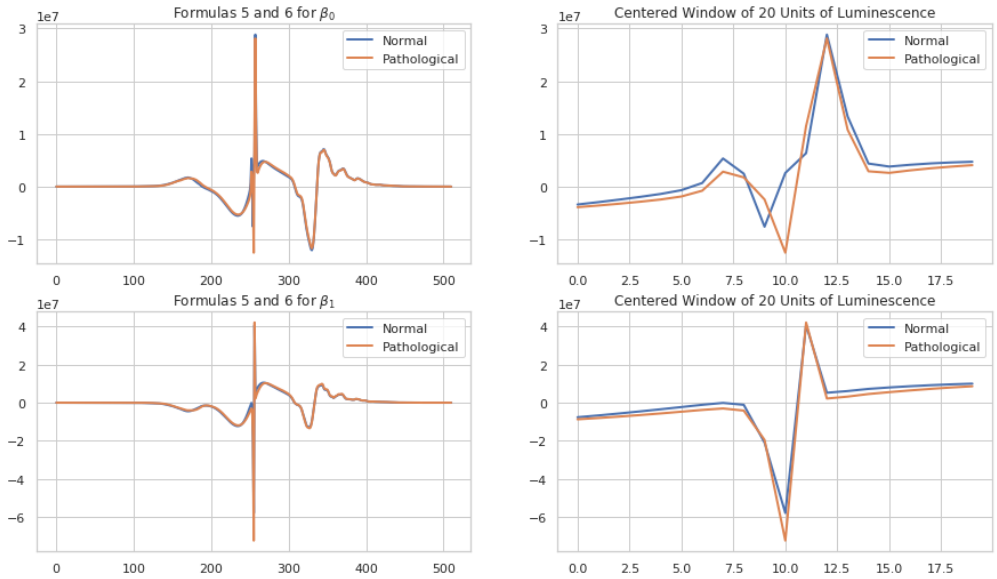

Figure 3.8: Resulting waveforms from applying Formulas 3.4 and 3.5 to β_0 and β_1 values. A centered window of 20 units of luminescence has been added for a granular visualization of the region of interest.

complexes, representing binarized images from the eye fundus of normal and pathological images, is granular enough to detect clinically relevant differences between them.

Once there is evidence that computational topology, through homological tools, is able to detect differences between images of normal and pathological eye fundus images, the next steps taken on this project are directed towards performing image quality assessment and, at one point modeling normality and pathology as showed on images of the eye fundus, in the context of diabetic retinopathy.

3.3.1 Modeling normality in digital eye-fundus images

In order to keep this method clinically relevant, we are following the way a fundus eye image is evaluated by a clinician:

1. Automatic selection of significant regions where information is found (background extraction).
2. Anatomical landmarks identification.
3. Identification of pathological changes.

These steps can be translated into processes of the method as shown in Figure 3.9.

Figure 3.9: Subprocesses according to clinical approach.

In order to approach the first step shown in Figure 3.9 a summary of the process is shown in Figure 3.10. This process uses elements from homology to guide the selection of optimal parameters in the algorithm, from now on called TRBE (Topology Regulated Background Extraction).

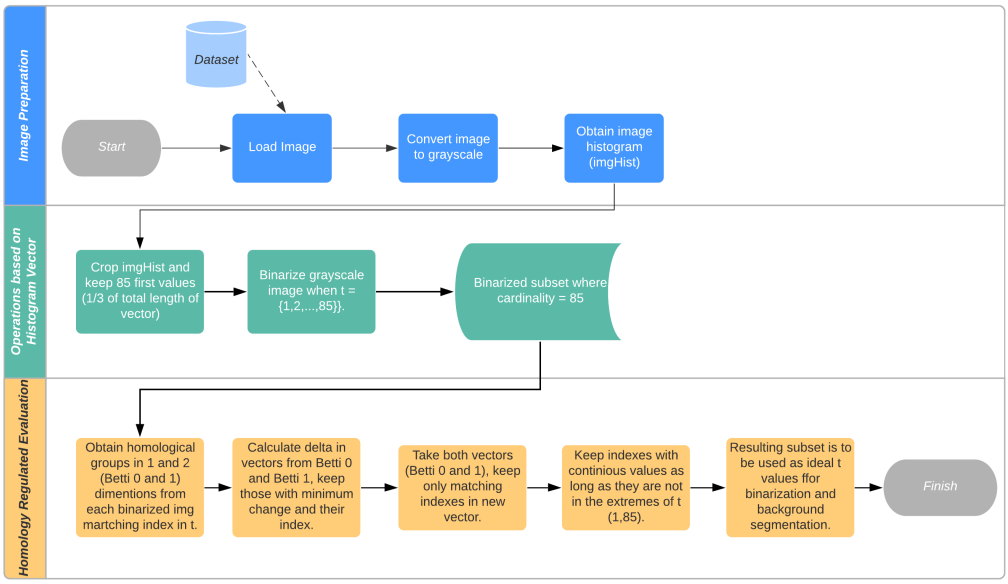

Figure 3.10: Topology Regulated Background Extraction (TRBE) Process.

Algorithm 1 presents a general approximation to a background extraction in generic images, it takes as inputs a grayscale image A and a threshold value t for the creation of a mask. The challenge with having a static threshold is that a single static value will not be adequate for all the images in the dataset. For this reason, an approach calculating homology groups of the resulting masks to evaluate suitability of the results is proposed to fine tune Algorithm 1.

Algorithm 1 downsizes A and generates the binarized image with a smaller image, then it returns the output to the original size of A, in order to lower computational time.

Algorithm 1: `maskBack`. Background extraction algorithm

input : An image matrix $A^{m \times n}$ of a grayscale eye fundus. A threshold integer value t.

output: Image matrix $M_A^{m \times n}$ representing background when $M_A(i,j) = 0$ and foreground when $M_A(i,j) = 255$

```
1 begin
2     for i ← 0 to m − 1 do
3         for j ← 0 to n − 1 do
4             if A(i, j) ≥ t then M_A(i, j) = 255;
5             else M_A(i, j) = 0;
```

Where:

- m = width of A.
- n = height of A.
- m_b = width of B.
- n_b = height of B.

Generation of ground truth

For the evaluation of the results a manual segmentation of the eye fundus was performed in each of the subsets of Normal and Abnormal images for both APTOS and MESSIDOR datasets. Given that the area with information of interest in an eye fundus image is delimited by a circle, a circular mask was implemented (Figure 3.11) to obtain these segmentations to be used as ***ground truth*** for the following steps in the analysis.

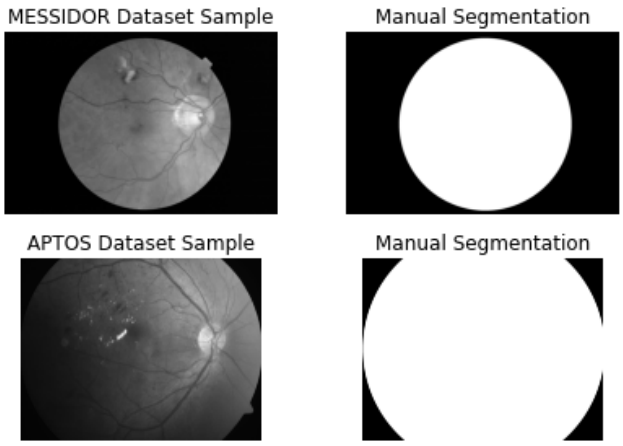

Figure 3.11: Examples of mask resulting from a manual segmentation on images from MESSIDOR and APTOS, notice that the masks are missing the characteristic protrusion on the image generated by the optical sensor, this is true for all masks used as ground truth.

Mean Squared Error (MSE)

This metric is used to compare between the output of TRBE generated to the ground truth as well as to other methods published in the literature, if needed.

The Mean Squared Error calculates the average squared difference between the estimated values and the actual value. It is always non-negative where values closer to zero are indicative of less difference between teh calculated and actual values. For 2d-arrays, such as grayscale images, MSE is calculated as shown in Formula 3.6:

$$\mathcal{MSE} = \frac{1}{mn}\sum_{i=0}^{m-1}\sum_{i=0}^{n-1}[A(i,j) - B(i,j)]^2 \tag{3.6}$$

Where:

- m =height in pixels of both images (they both have to share the same size).
- n =width in pixels of both images.
- A, B =image matrices to be compared.

3.3.2 Optimization through an iterative process

In order to move towards the identification of a metric to be used in this process, an iterative approach to the optimization of the optimal β_0 and β_1 values was performed on the subset of images where there were manual segmentations (*ground* truth) available.

The approach consisted of iterating on the whole depth of luminescence and using each available value for the parameter t for each image. Given that both Aptos and

Messidor datasets contain 8-bit images, the range of values available ended up being $t = \{0, 1, \ldots, 255\}$. At each binarization the other parameters were also calculated (β_0, β_1, MSE). Then the minimum MSE was selected along with the corresponding subset of complementary values (t, β_0, β_1) and saved to an array with the results from the rest of the images in the dataset. Figure 3.12 shows the visualization of the results in an example from both datasets.

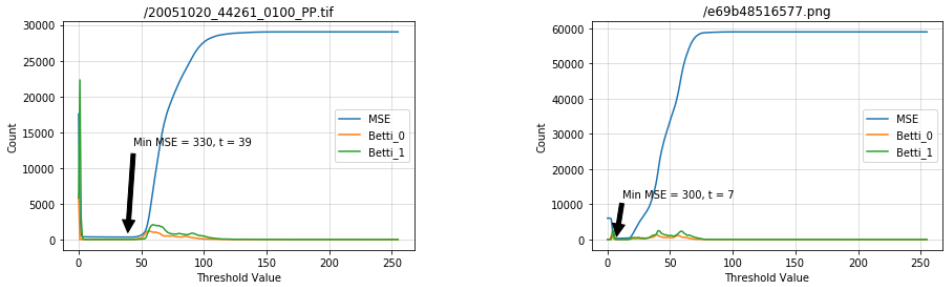

(a) Example from the MESSIDOR dataset. **(b)** Example form the APTOS Dataset

Figure 3.12: Examples of the results from the iterative optimization process.

It is evident that the visualization of the region where the closest mask to the manual segmentation is not optimal. In order to fix this all three vectors were projected to the same range through normalization, following Formula 3.7:

$$X'_i = \frac{X_i - X_{min}}{X_{max} - X_{min}} \tag{3.7}$$

Where:

- X'_i = the $i-th$ element of the normalized vector.
- X_i = the $i-th$ element of the original vector.
- X_{min} = the minimum value of the original vector.
- X_{max} = the maximum value of the original vector.

The results are presented in Figure 3.13, eventhough more details are visible with this approach, the region where the optimal subset of t is found is not clearly seen. In order to maximize the visualization of such region both axis were projected in logarithmic scale, this can be seen in Figure 3.14

Given that the interest of the evaluation is to focus on β_0 and β_1 indicators so the method can be expanded to images without a manual segmentation, the visualization of logarithmic scales on both axes without normalizing the values contained on the indicator vectors is proposed as the ideal to run the analysis for all manually segmented images. The example of this visualization using the same two images previously shown can be seen on Figure 3.15.

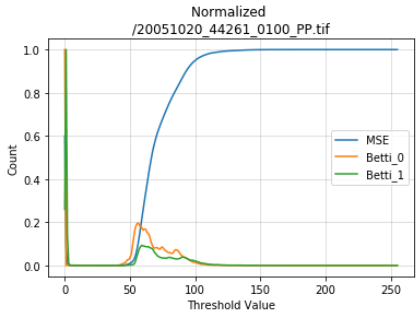

(a) Example from the MESSIDOR dataset.

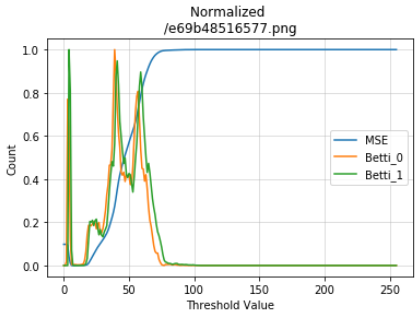

(b) Example form the APTOS Dataset

Figure 3.13: Examples from Figure 3.12 with normalized values.

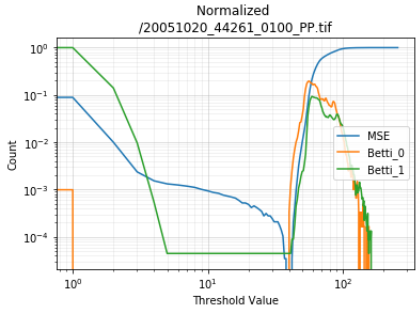

(a) Example from the MESSIDOR dataset.

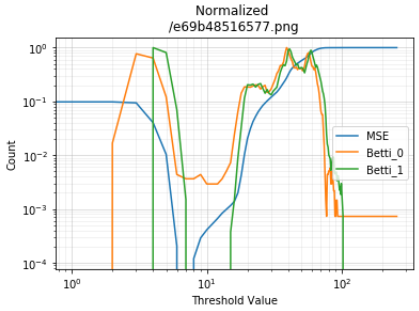

(b) Example form the APTOS Dataset

Figure 3.14: Examples from Figure 3.13 with axis in logarithmic scale.

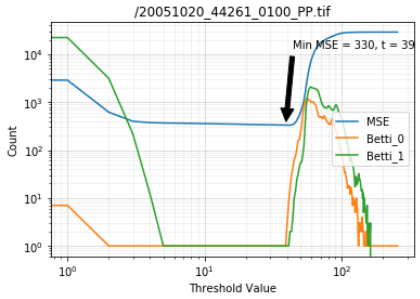

(a) Fig.3.12a with logarithmic scale.

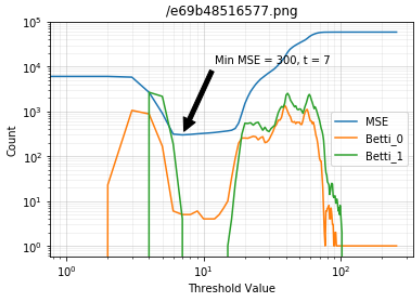

(b) Fig. 3.12b with logarithmic scale.

Figure 3.15: Examples of iterative optimization process visualized with logarithmic scales on both axis.

A pattern can be seen on Subfigures 3.14a, 3.14b, 3.15a, and 3.15b where β_0 and β_1 values seem to reach a local minima plateau around the region of minimal values for MSE. **If this pattern is evident for the rest of the images in both datasets**

then finding such plateau for β_0 and β_1 values could be used to select a subset of candidates for t in TRBE. The visualization of all images used for this stage in the process can be accesed through the follwoing links:

- Messidor Normals.
- Messidor Abnormals.
- Aptos Normals.
- Aptos Abnormals.

Subseting thresholding values

Once the results from Subsection 3.3.2 are obtained for β_0, β_1 and MSE, the following step is to select a subset of t corresponding to the local minima plateau region mentioned at the end of the previous Subsection. Given that the local minima plateau will be located towards the lower values of luminescence, only this section of the vector is of interest out of all the luminescence depth. For the previous reason the luminescence vector is split into four sections and the one with t values closer to 0 is selected. Therefore, for the following steps we will be working with the subset $t = \{1, 2, \ldots, 64\}$. The results of running the above process are shown on Figure 3.16.

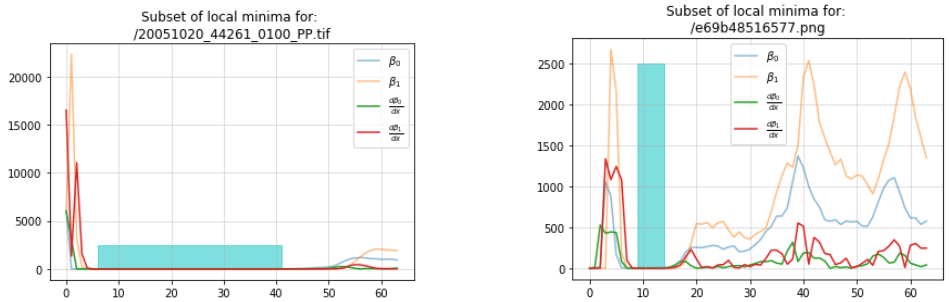

(a) **(b)**

Figure 3.16: Results of local minima found on images from Figure 3.12, region highlighted on cyan.

For Subfigures 3.16a and 3.16b the values within the cyan bands are as follows:

- Subfigure 3.16a:
  - $t = \{6,7,8,9,10,11,12,13,14,15,16,17,18,19,20,21,22,23,24,25,26,27,28,29,30,31, 32,33,34,35,36,37, 38,39,40,41\}$
- Subfigure 3.16b:
  - $t = \{9,10,11,12,13,14\}$

Testing TRBE with APTOS images

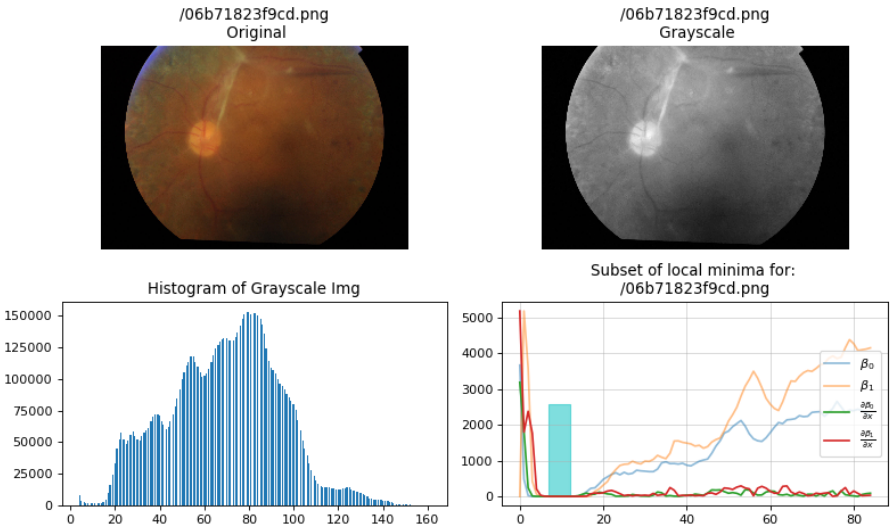

Figure 3.17: Local minima when $t = \{7, 8, 9, 10, 11, 12\}$

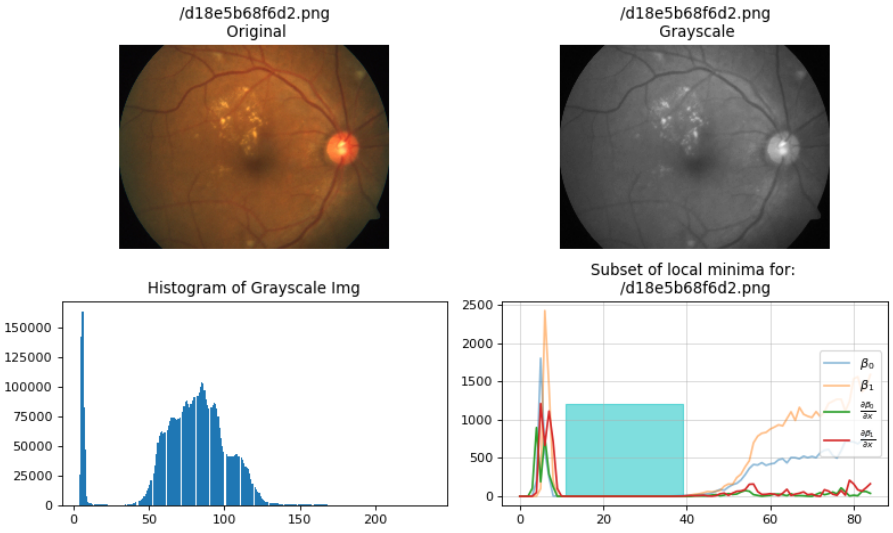

Figure 3.18: Local minima when $t = \{11, 12, ..., 39\}$

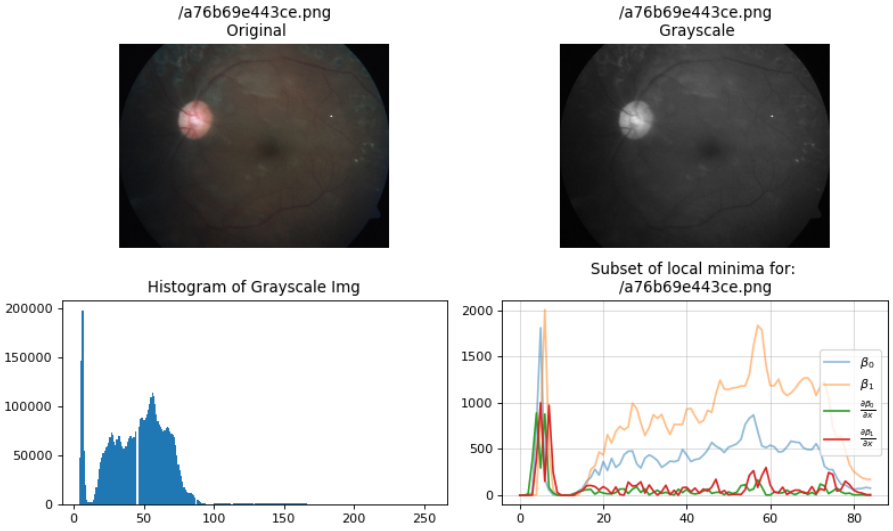

Figure 3.19: Local minima when $t = \{\emptyset\}$

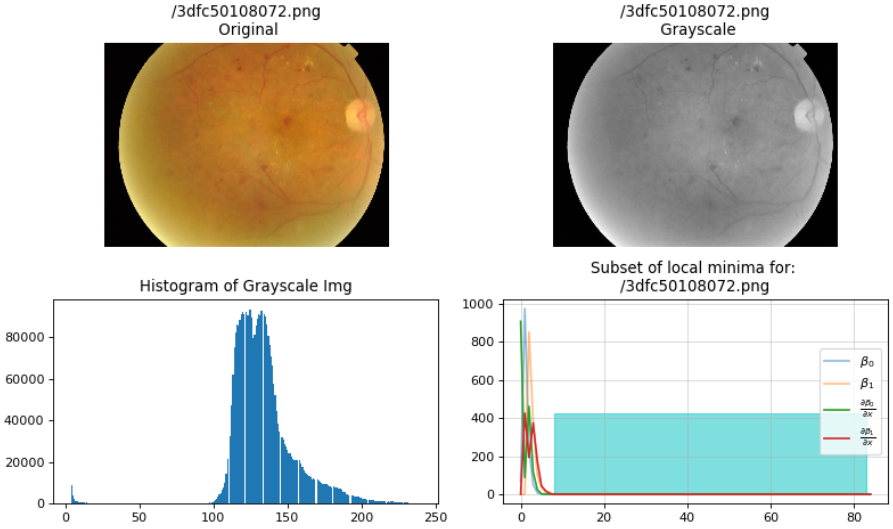

Figure 3.20: Local minima when $t = \{1, 2, \ldots, 83\}$

Otsu's method for dynamic background extraction for performance comparison

This method is an adaptive thresholding approach to the binarization of an image. It achieves this by iterating through all luminescence values as possible thresholds and finding the optimal option so that within class variance (V_W) is minimal [92].

The first step in the method is to obtain an image histogram from a grayscale image. As shown in Figure 3.21.

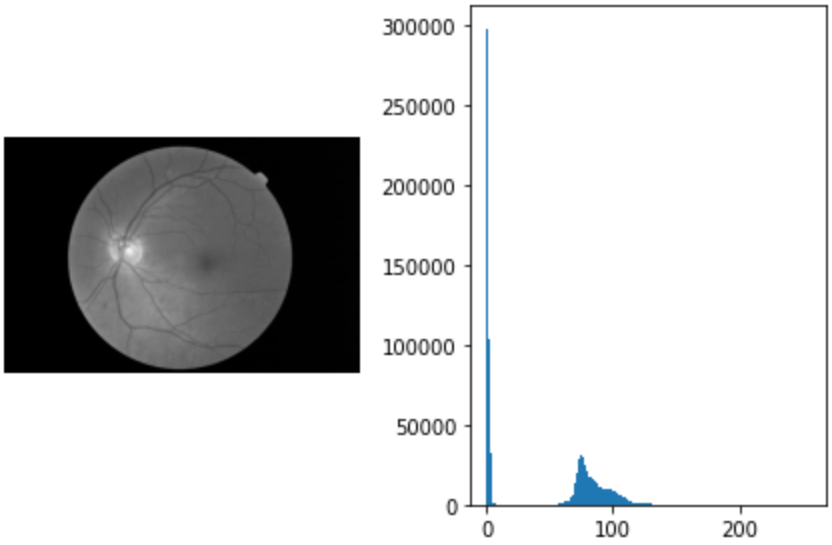

Figure 3.21: Eye fundus image in grayscale format and the resulting image histogram.

The next step in the method is to calculate within-class variance (V_w) [93], where the goal is to find the threshold producing the minimal V_w, following formula 3.8:

$$\mathcal{V}_w = \sum_{i=0}^{N} (W_i * \sigma_i^2) \tag{3.8}$$

Where:

- $W_i = X_i \ / \ N$
- $X_i =$ pixels in class i
- $N =$ total number of pixels.
- $\sigma^2 = \frac{\sum_{i=0}^{N}(X_i - \mu)^2}{N}$

Another way of approaching this problem is by finding the threshold producing the maximum between-class variance (V_b) [93], which is the variance between two classes. Therefore, if pixels are classified in N classes or categories then the between-class variances can be deducted as following:

$$\mathcal{V}_b = V_T - V_w \tag{3.9}$$

Where:

- V_b = between-class variance
- V_T = total variance
- V_w = within-class variance

Figure 3.22 shows the result of apllying Otsu's method to the image in Figure 3.21 using V_b, for details of the implementation used see [94].

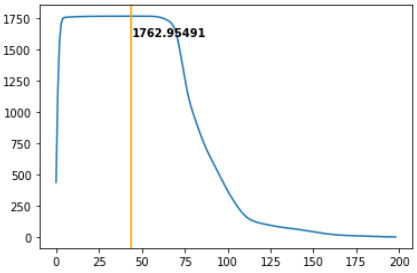

(a) V_b values with maximum indicated.

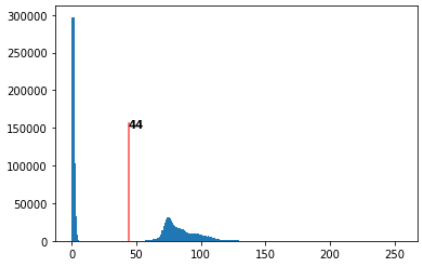

(b) Histogram with optimal threshold.

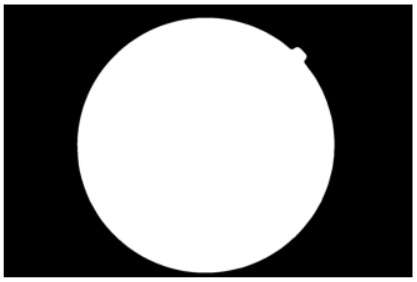

(c) Resulting mask.

Figure 3.22: Results obtained with Otsu's method, showing image histogram and threshold used to generate binarized image.

3.3.3 Luminescence-based filtration of a cubical complex derived from a digital image

A grayscale image comes with a natural filtration embedded in the grayscale values of its pixels. Let $\mathcal{K}$ be the cubical complex built from the image I. Then, let:

$$\mathcal{K}_i := \{\sigma \in \mathcal{K} | \mathcal{J}'(\sigma) \leq i\} \tag{3.10}$$

for the $i-th$ sublevel set of $\mathcal{K}$. The set $\{\mathcal{K}_)\}_{i\in\mathcal{J}}$ defines a filtration of cubical complexes, indexed by the value of the grayscale function $\mathcal{J}$.

All images in the EyePACS dataset are in the 8−bit format, therefore the grayscale versions have a depth of luminescence of 256 values (0 for absolute black, 255 for

absolute white, and shades of gray for the corresponding values in between them). According to the previous information and following Formula 3.10, a natural filtration with 256 sublevels can be extracted from these images once they are interpreted as 2−cubical simplices given that $i = \{0, 1, 2, \ldots, 256\}$.

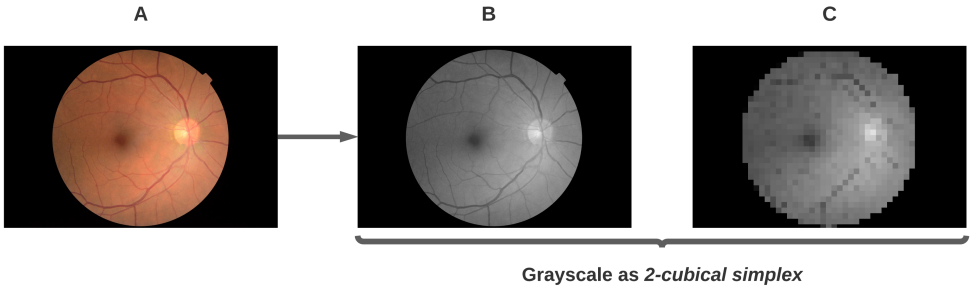

Figure 3.23: Example of the process of transforming a color eye fundus image from the EyePACS dataset (A) to the grayscale version (B) and a simplification to show how pixels in a grayscale image fulfill the definition of a cubical complex in 2 dimensions (C).

Component C in Figure 3.23 exemplifies the issue of a pixelated version of component B where pixels are visible as cells in a 2D grid (the image matrix) and naturally interpretable as 2−cubes (see Figure 3.23), each one of the four sides of a pixel (lines delimiting each cell in the image matrix) can be interpreted as a 1−cube (see Figure 3.23). Following a combinatorial approach, we obtain a mathematical object representing the digital grayscale image on which Topological Data Analysis can be performed, namely the $2D$ cubical complex.

3.3.4 Cubical Filtrations

The steps to obtain a filtration from a grayscale image are as shown in Equation 3.11:

$$\text{Image} \rightarrow \text{Cubical complex} \rightarrow \text{Sublevel sets} \rightarrow \text{Filtration} \tag{3.11}$$

Figure 3.24 shows a filtration of a cubical complex induced by the grayscale values contained in the image matrix and the corresponding barcode, notice that the barcode only has one element per homological group (0 and 1 dimensional topological characteristics), this information is reported in the form of Betti numbers (β_i); where β_0 = the number of 0−dimensional topological characteristics or connected components (connected complete black pixels for the use case of this work) at a specific sublevel filtration, β_1 = the number of 1− dimensional topological characteristics or holes inside connected components (complete white pixels inside components made of black pixels), this analysis is called persistent homology (PH) [95]. The figure presents an oversimplified example. Real data will typically have multiple bars per homological group in a filtration as seen in Figure 3.24.

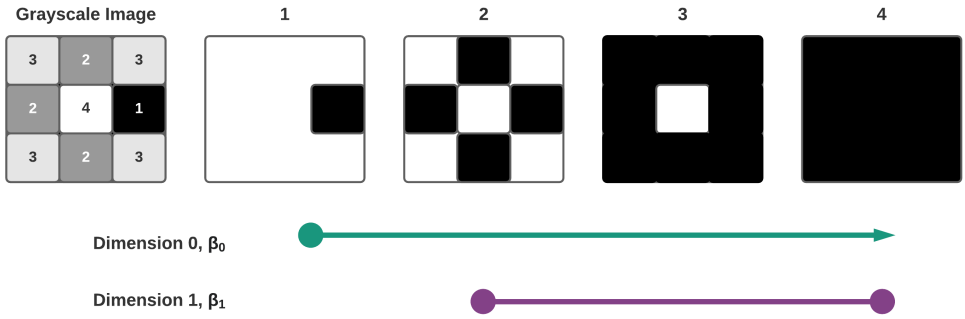

Figure 3.24: Induced filtration of a 3×3 grayscale image matrix and the correspondent barcode for β_0 and β_1. Using a luminescence depth of 4 elements, $L = \{1, 2, 3, 4\}$, to simplify the example.

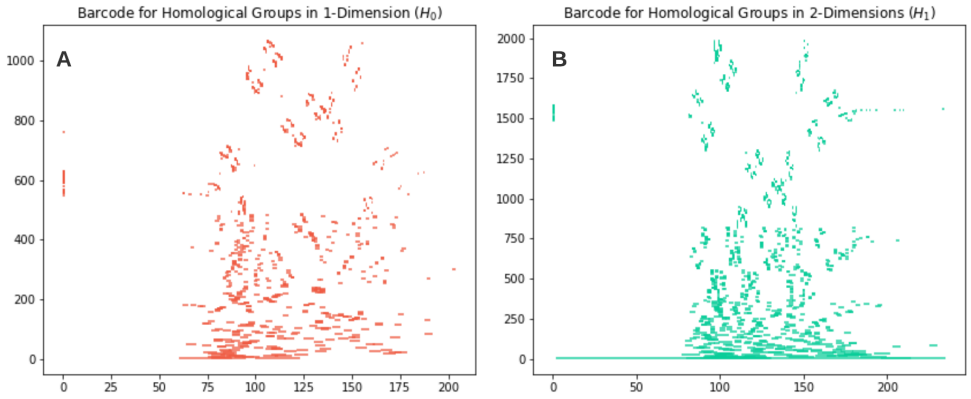

Figure 3.25: Corresponding bar codes for 0 and 1-dimensional homological groups (A,B) of Figure 3.23-B. Displayed on the x axis are the filtrations sublevels (since it is an 8−bit image there are 256 sublevels available). The y axis shows a count of structures per sublevel in the form of bar codes. Each barcode starts and finishes at the birth and dead sublevel value for the structure it represents.

Figures 3.24-A and 3.24-B show at least one bar that persists longer than the rest for each dimension (H_0 and H_1). Figure 3.26 explores in a visualization some of the sublevel sets (grayscale values) corresponding to each bar per dimension.

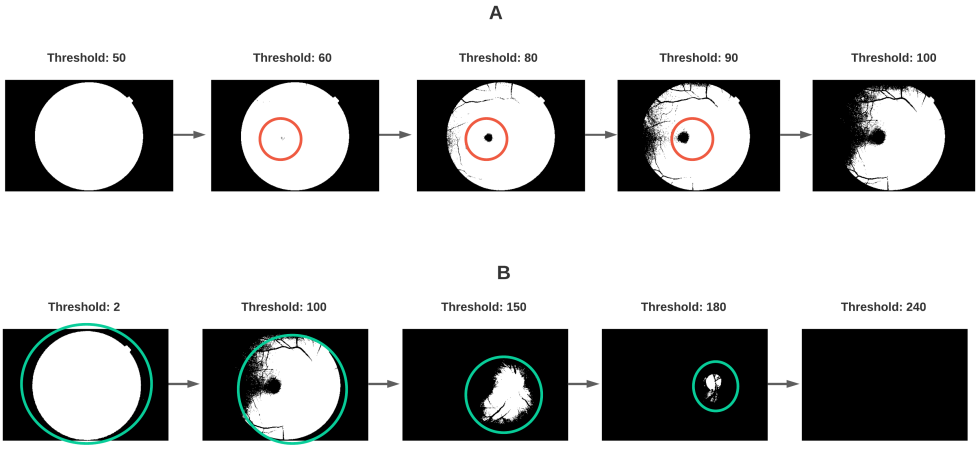

Figure 3.26: Visualization of binarized images from Figure 3.23-B thresholded at grayscale values contained in the topological elements persisting for the largest amount of sublevel sets in the filtration represented by barcodes in Figure 3.25. Done for the bar in H_0 (A) and H_1 (B).

By binarizing Figure 3.23-B using threshold values contained in the longest bar of Figure 3.25, we can appreciate the resulting series in Figure 3.26-A; a connected component of clinical relevance appears at around a grayscale value of 60 and persists until a value of 90 before merging into a larger unified component with the background at around a grayscale value of 100. Interestingly this spot, connected component, or $0-$dimensional homological group is consistent with the macula and fovea as anatomical landmarks. It is here at this point that the topological results begin to connect with clinical meaning for the domain of which the data comes from, in this case eye fundus images and the diagnostic process in which they are used

Figure 3.25-B also shows a $1-$dimensional homological group persisting significantly more than the rest in the filtration (from 2 to over 200). This means that there must be a recognizable hole (H_1 homological group) when binarizing the image using threshold values contained in the bar for such homological group. Figure 3.26-B shows a series of binarized images using some of the values in the range of 2 to 240 and visually confirms the topological findings with a persistent hole which first represents all the area of the camera sensor in which the information of the eye fundus image is contained and shrinks until the anatomical region where the optic disk would be expected to be. This is consistent with clinical practice where the area of the optic disk is typically regarded as the brightest in a healthy eye fundus evaluation. Again, connecting $1-$dimensional topological structures to clinical meaning.

3.3.5 Topological Indicators Derived from Digital Images

Once an eye fundus image has been interpreted as a $2D$ cubical complex and a corresponding PH analysis has been performed, as shown in Subsection 3.3.4, the results must be vectorized to provide an input that machine learning (ML) algorithms can take for classification purposes. For this work ML algorithms are used to perform Image Quality Assessment (IQA) of the eye fundus images. This section presents details dealing with the process of vectorization of topological results represented by persistence diagrams.

Figure 3.27 shows a representation of the pipeline used in this work to perform Topolog-ical Data Analysis (TDA) and obtain a vectorized representation to feed a ML classificator (in this case a Logistic Regression), each eye fundus image was first converted from color to grayscale (Figure 3.23) and then, entered the pipeline described in this Section.

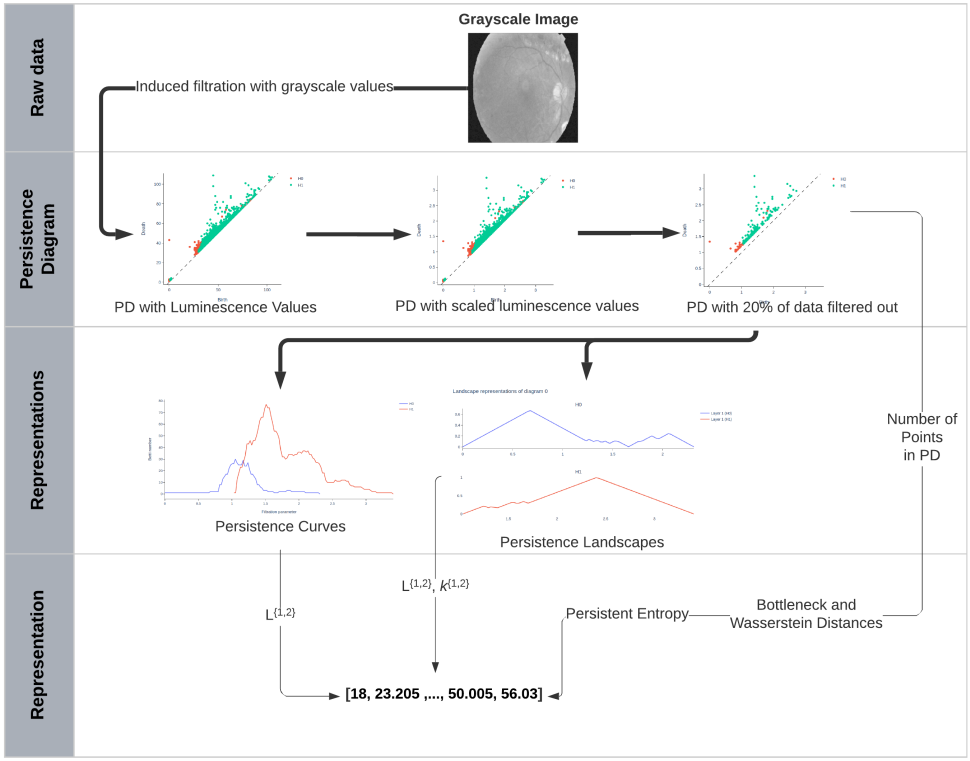

Figure 3.27: Representation of pipeline for extraction of topological descriptors of eye fundus images.

3.3.6 Persistence Diagrams

A persistence diagram (PD) is a visual representation of a set of points $\{(b, d)|b, d \in \mathbb{R}^2\}$ and $d > b$, where d = death of the topological feature and b = birth of the topological feature [14]. In order to be able to feed topological features represented in a persistent diagram to a machine learning algorithm they must be vectorized.

Figure 3.28 shows the corresponding PD for 0 and 1−dimensional topological characteristics obtained from a PH analysis of Figure 3.23-B. Notice that the results are consistent with those observed in the codebars in Figure 3.25, only that it is easier to identify persistent characteristics.

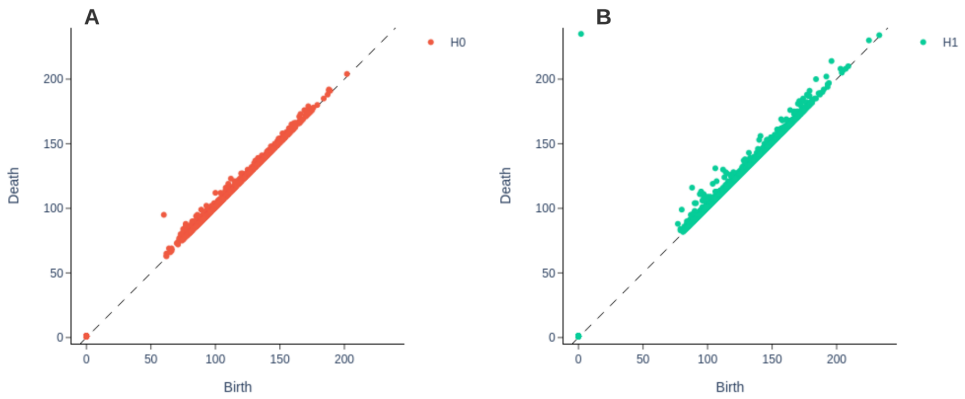

Figure 3.28: Persistence Diagrams (PDs) corresponding to barcodes in Figure 3.25, notice that the same information is presented in a more understandable manner, where the diagonal line represents the birth value and the points above the diagonal represent the dead value of a given topological characteristic. PDs facilitate the identification of noise versus relevant topological characteristics.

3.4 Vectorization of results in Persistence Diagrams

The following paragraphs explain how results shown in a PD are vectorized for the analysis implemented in this work. From this point on eye fundus images are represented by their corresponding PDs over which the rest of the analysis is performed.

3.4.1 Persistent Entropy of Persistence Diagrams

It is an intuitive measure of the entropy of the points in a persistence diagram. It results from extracting the Shannon entropy of the persistence (lifetime) of all cycles (topological structures) [37,38].

Let $D = \{(b_i, d_i)\}_{(i \in I)}$ be a persistence diagram with each $d_i < +\infty$, where $b_i =$ the $i-th$ topological birth point of the structure, and $d_i =$ the $i-th$ topological dead point of the structure. The persistence entropy of D is defined in Equation 3.12.

$$PE(D) = \sum_{i=1}^{n} \frac{l_i}{L(B)} log\left(\frac{l_i}{L(B)}\right) \tag{3.12}$$

Where: $l_i \coloneqq d_i - b_i$ and $L(B) \coloneqq l_1, \ldots, l_n$, as the sum of all the persistences.

3.4.2 Bottleneck Distance

Let X and Y be two persistence diagrams. To define the distance between them, we consider bijections $\eta : X \to Y$ and record the least upper bound (sup) of the distances between corresponding points for each. Measuring distance between points $x = (x_1, x_2)$ and $y = (y_1, y_2)$ with L_∞-norm: $\|x - y\|_\infty = max\{|x_1 - y_1|, |x_2 - y_2|\}$ and taking the greatest lower bound (inf) over all bijections, we get the bottleneck distance between diagrams [96], as shown in Equation 3.13.

$$W_\infty(X, Y) = \inf_{\eta: X \to Y} \sup_{x \in X} \|x - \eta(x)\|_\infty \tag{3.13}$$

A drawback of the bottleneck distance is that it is insensitive to details of the bijection beyond the furthest pair of corresponding points.

3.4.3 $p-$Wasserstein Distance

The $p-$Wasserstein distance between X and Y for any positive real number p, takes the sum of $p-$th powers of the L_∞ distances between corresponding points, again minimizing over all bijections, as shown in Equation 3.14.

$$W_p(X, Y) = \left[\inf_{\eta: X \to Y} \sum_{x \in X} \|x - \eta(x)\|_\infty^q\right]^{1/p} \tag{3.14}$$

It is also known as the Earth´s movers distance because, intuitively, it can be interpreted as the minimum energy cost of moving a pile of dirt in the shape of one probability distribution to the another. Therefore, the $p-$Wasserstein distance measures the similarity between two presistence diagrams using the sum of al edge lengths [97].

3.4.4 Persistence Landscape

The $k-$th persistence landscape of a barcode $\{(b_i, d_i)\}_{i=1}^n$ in the function $\lambda_k : \mathbb{R} \to [0, \infty)$ is the $k-$th largest value of $\{f_{(b_i, d_i)}(x)\}_{i=1}^n$, with:

$$f_{b,d}(x) = \begin{cases} 0 & \text{if } x \in (b, d) \\ x - b & \text{if } x \in \left(b, \frac{b+d}{2}\right) \\ -x + d & \text{if } x \in \left(\frac{b+d}{2}, d\right) \end{cases} \tag{3.15}$$

The parameter k is called the layer. In this work we consider curves obtained when $k \in \{1, 2\}$ [98, 99].

3.4.5 Betti Curves

For the porpuse of this work, the Betti curve $B_n : I \to \mathbb{R}$ of a barcode $D = \{(b_i, d_i)\}_{j \in I}$ is the function that returns for each step $i \in I$, the number of bars (b_j, d_j) that contain j, as shown in Equation 3.16.

$$i \mapsto \#\{(b_j, d_j)\}, i \in (b_j, d_j) \tag{3.16}$$

Where # stands for cardinality.

3.4.6 Gaussian Kernel

By placing Gaussians of standard deviation σ over every point of the persistence diagram and a negative Gaussian of the same standard deviation in the mirror image of the points across the diagonal, the output of this operation is a real-valued function on $\mathbb{R}^2$. For this work, we use $\sigma \in \{1.6, 3.2\}$ [100].

3.4.7 Number of Points in Persistence Diagram

This indicator refers to the number of off-diagonal points in a given persistence diagram, per homology dimension. Given a persistence diagram consisting of birth–death–dimension triples $[b, d, q]$, subdiagrams corresponding to distinct homology dimensions are considered separately, and the respective numbers of off-diagonal points are counted and reported as the result.

3.5 Machine Learning Classifiers

Once the topological indicators are vectorized as mentioned in Section 3.4, the dataset is ready to be processed by standard machine learning classifiers. For this work, we explored the following algorithms:

- Support vector machine,
- Classification tree,
- $k-$nearest neighbors,

- Random forest,
- Logistic regression,
- Multilayerd perceptron.

For these initial explorations, the authors used Orange3 [101], selecting the default hyperparameters proposed by the software for each of the algorithms. Then, a subset of algorithms was selected based on their performance and evaluated in more depth in order to choose the classifier to use for this work.

3.6 Metrics for Evaluation of Performance of Classification Algorithms

Given a confusion matrix, as shown in Figure 3.29, in the context of a binary classification, the following indicators are identified:

- **True positives (TP):** entities classified by the algorithm as true to the label evaluated when the reference is also true.
- **True negatives (TN):** entities classified by the algorithm as true to the label evaluated when the reference is false.
- **False positives (FP):** entities classified by the algorithm as false to the label evaluated when the reference is also false, also known as Type I Error.
- **False negatives (FN):** entities classified by the algorithm as false to the label evaluated when the reference is true, also known as Type II Error.

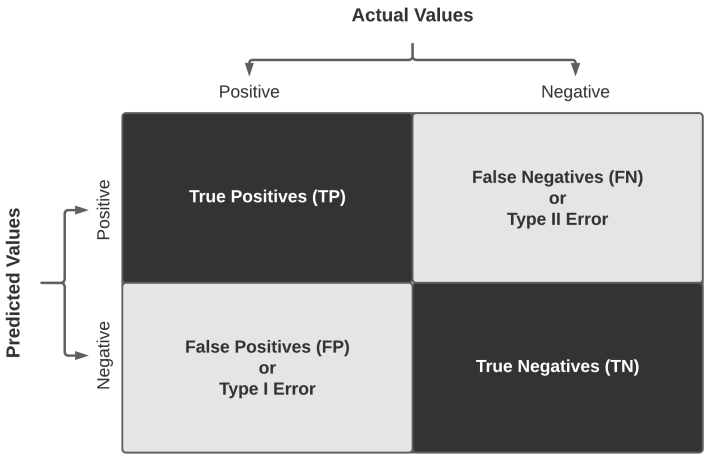

Figure 3.29: Visualization of a generic confusion matrix.

The following metrics are used to report on algorithm performance on this work [102]:

Accuracy

This metric answers the following question: overall, how often is our model correct? It is calculated using Equation 3.17:

$$Accuracy = \frac{TP + TN}{TP + TN + FP + FN} \tag{3.17}$$

It does not work well with class imbalance, nor does it give detailed information about the application of the problem.

Precision

This metric answers the following question: what is the ratio between the true positives and all the positives? It is calculated using Equation 3.18:

$$Precision = \frac{TP}{TP + FP} \tag{3.18}$$

This metric helps when the impact (defined by the domain of the data) of false positives is significantly high.

Recall

This metric answers the following question: what is the measure of our model correctly identifying true positives? It is calculated using Equation 3.19:

$$Recall = \frac{TP}{TP + FN} \tag{3.19}$$

This metric helps when the impact (defined by the domain of the data) of false negatives is significantly high. It is also known as sensitivity or true positive rate (TPR).

F1-score

This metric is a combined measure of precision and recall. Therefore, a relatively high F1-score will mean that there are low false positives and low false negatives in the results generated by the classifier. It is calculated using Equation 3.20:

$$F1 = 2 \times \frac{\frac{TP}{TP+FP} \times \frac{TP}{TP+FN}}{\frac{TP}{TP+FP} + \frac{TP}{TP+FN}} = 2 \times \frac{precision \times recall}{precision + recall} \tag{3.20}$$

Receiver-operating characteristic (ROC) curve:

This curve is considered a comprehensive performance measure and it is obtained by visualizing the true positive rate (TPR) versus the false positive rate (FPR), this last one is calculated following Equation 3.21:

$$FPR = 1 - Specificity = 1 - \frac{FP}{FP + TN} \tag{3.21}$$

Area under the curve (AUC):

Once a ROC curve is generated, the area under such curve can also be used to measure the performance of the algorithm. The AUC shows the probability that a randomly classified positive sample becomes a higher score than a randomly classified negative sample. It can be expressed as shown in Equation 3.22:

$$AUC = P(X_{pos} > X_{neg}) \tag{3.22}$$

Matthews correlation coefficient (MCC):

Typically used to evaluate the performance of classifiers when dealing with data with an unbalanced proportion of elements in each of the labels of the target variable [103], it is obtained by following Equation 3.23:

$$MCC = \frac{(TP \times TN) - (FP \times FN)}{\sqrt{(TP + FP)(TP + FN)(TN + FP)(TN + FN)}} \tag{3.23}$$

Chapter 4

Results

4.0.1 Performance evaluation of TRBE *versus* Otsu's method for background extraction in eye fundus images

Eventhough a through analysis is in the making, preliminar results show that TRBE is much rubost to noise and low quality images than Otsu's method. Nevertheless, a detailed analysis is on the making.

	Img	Otsu tTRBE	tMSE	OtsuMSE	TRBEClosest to Manual Seg
0	/d18e5b68f6d2.png	46.0	25.0	759	487TRBE
1	/4818672273af.png	38.0	28.0	1262	1210TRBE
2	/c1e6fa1ad314.png	32.0	21.5	441	377TRBE
3	/8ab8d9b3ce3f.png	63.0	46.5	285	250TRBE
4	/c613db1cab27.png	46.0	36.5	345	311TRBE
5	/4e43d05cc2ef.png	40.0	26.0	628	591TRBE
6	/82bb8a01935f.png	42.0	26.0	1259	1213TRBE
7	/282bc792d23a.png	46.0	33.5	273	223TRBE
8	/f69400b316a7.png	37.0	27.0	252	235TRBE
9	/c252da9b41d8.png	54.0	41.5	256	209TRBE
10	/757572337fd0.png	45.0	36.0	323	297TRBE
11	/8cb6b5b2f19c.png	39.0	27.0	543	490TRBE
12	/6e73acb2cf60.png	40.0	24.0	362	326TRBE
13	/237c078d00fc.png	74.0	22.0	17736	362TRBE
14	/a476fd984005.png	32.0	22.5	1450	1383TRBE
15	/e55188915f9d.png	48.0	27.5	409	363TRBE
16	/e9ff9352ccb3.png	44.0	27.5	1409	1348TRBE
17	/fe0fc67c7980.png	32.0	19.0	1497	1367TRBE
18	/d91273efb92a.png	56.0	46.0	361	340TRBE
19	/b89938407ee6.png	77.0	16.5	27935	289TRBE
20	/98e8adcf085c.png	24.0	16.0	241	224TRBE
21	/b07bc463b718.png	54.0	20.0	29278	244TRBE

22	/8a9bef2fbd4e.png	31.0	19.5	385	339TRBE
23	/5265dc9acdf8.png	53.0	44.5	229	198TRBE
24	/f901d460517c.png	40.0	16.0	3306	891TRBE
25	/0dce95217626.png	41.0	27.0	254	229TRBE
26	/91b6ebaa3678.png	42.0	26.0	295	246TRBE
27	/a14bbd9a583e.png	49.0	34.5	468	426TRBE
28	/fa59221cf464.png	34.0	23.0	2386	2318TRBE
29	/dc6fa1b38b83.png	66.0	27.0	15860	324TRBE
30	/e868c3da340b.png	57.0	46.5	362	319TRBE
31	/2a5a8b744f08.png	36.0	23.0	482	438TRBE
32	/bfd5c0e55420.png	57.0	44.0	292	278TRBE
33	/999115d9386b.png	47.0	34.5	307	273TRBE
34	/6b00cb764237.png	40.0	29.5	540	505TRBE
35	/0ada12c0e78f.png	72.0	16.0	37583	408TRBE
36	/849a91e9ab28.png	41.0	31.5	375	342TRBE
37	/423abbaa5fad.png	34.0	21.5	349	328TRBE
38	/fd62bd0db4f1.png	57.0	20.5	10551	303TRBE
39	/c8fc0df22999.png	46.0	33.5	463	433TRBE
40	/fe37f4492920.png	56.0	41.0	466	430TRBE
41	/b95d4dd8e5e2.png	59.0	46.0	539	496TRBE
42	/b87f9c59748b.png	55.0	31.0	1353	193TRBE
43	/27e4c800a449.png	31.0	19.0	223	205TRBE
44	/fcc6aa6755e6.png	37.0	9.0	5767	2215TRBE
45	/e1e490773462.png	40.0	31.0	1356	1310TRBE
46	/b1f4122fd36a.png	44.0	32.5	512	451TRBE
47	/5e7db41b3bee.png	25.0	13.0	410	234TRBE
48	/248139c423c4.png	71.0	46.5	329	228TRBE
49	/f0c0f7b5e820.png	41.0	20.5	890	568TRBE
50	/8bdb891661a8.png	68.0	16.5	26823	362TRBE
51	/a56230242a95.png	57.0	44.5	547	469TRBE
52	/5b76117c4bcb.png	48.0	21.5	1312	430TRBE
53	/278aa860dffd.png	38.0	26.0	510	493TRBE
54	/962cf85e4f6d.png	58.0	43.5	415	385TRBE
55	/11242a67122d.png	38.0	23.5	347	293TRBE
56	/295fdc964f6e.png	38.0	26.0	477	459TRBE
57	/86d6808f0609.png	34.0	19.5	434	391TRBE
58	/8f1e7433a95d.png	44.0	32.5	1295	1247TRBE
59	/1c5e6cdc7ee1.png	42.0	31.0	287	269TRBE
60	/000c1434d8d7.png	34.0	25.0	333	280TRBE
61	/7e9458de5707.png	34.0	19.5	330	315TRBE
62	/e7defafeb957.png	45.0	33.5	1253	1196TRBE
63	/6810410187a0.png	53.0	41.0	290	239TRBE
64	/0d310aba6373.png	48.0	24.5	1074	335TRBE

65	/12a82fc7d73e.png	40.0	30.0	1318	1265TRBE
66	/aa9cfe639ef1.png	43.0	29.5	1344	1315TRBE
67	/1b4625877527.png	46.0	33.0	443	389TRBE
68	/f03d3c4ce7fb.png	39.0	23.0	387	386TRBE
69	/b4f41b5bf0ef.png	37.0	24.0	401	399TRBE
70	/ba08cee68c71.png	37.0	23.5	394	351TRBE
71	/8fc09fecd22f.png	46.0	31.0	465	431TRBE
72	/44e0d56e9d42.png	50.0	39.5	358	319TRBE
73	/a15652b22ab8.png	39.0	22.0	521	470TRBE
74	/d364423ec6f9.png	57.0	42.0	242	213TRBE
75	/1a7e3356b39c.png	42.0	13.0	10516	1045TRBE
76	/a76b69e443ce.png	44.0	NaN	22192	58846Otsu
77	/803120c5d287.png	48.0	31.5	1254	1226TRBE
78	/46cdc8b685bd.png	38.0	24.5	353	278TRBE
79	/2376e5415458.png	64.0	21.5	16269	250TRBE
80	/b3d135bd3bb5.png	53.0	39.5	339	304TRBE
81	/3f752fcccec0.png	39.0	26.5	441	389TRBE
82	/281d7b7c7676.png	43.0	35.0	1100	1053TRBE
83	/236f56771ec6.png	31.0	19.0	206	194TRBE
84	/4a0bba3b7d83.png	51.0	38.0	365	336TRBE
85	/fc4d69128e7c.png	69.0	80.5	33383	37544Otsu
86	/70ed3ec68b94.png	46.0	37.0	302	261TRBE
87	/b498b84d383f.png	43.0	31.5	1195	1149TRBE
88	/3dfc50108072.png	68.0	45.5	408	370TRBE
89	/6666c4f18396.png	31.0	16.5	729	570TRBE
90	/e19936582c61.png	50.0	34.5	265	248TRBE
91	/4abca30b676b.png	60.0	41.5	427	403TRBE
92	/655cafb4c932.png	60.0	46.0	424	406TRBE
93	/ba4d2c4b3039.png	34.0	23.0	1333	1297TRBE
94	/f999c6921e6d.png	35.0	18.5	522	421TRBE
95	/92d8a7c8e718.png	75.0	30.5	14841	471TRBE
96	/06b71823f9cd.png	43.0	9.5	8812	1106TRBE
97	/5e7630f8438e.png	46.0	30.0	193	182TRBE
98	/7a238a1d3cf3.png	49.0	38.5	355	309TRBE
99	/85fce24084da.png	57.0	46.5	348	326TRBE
100	/7bc2e0fa3f72.png	38.0	13.5	16753	206TRBE

Table 4.1: Preliminary results of Otsu's method *versus* TRBE when compared to a manual segmentation as ground truth.

As shown in Table 4.1 TRBE shows to be a more robust method for dynamic background extraction than Otsu's method, specially when dealing with low quality images, which is the kind of images expected in community ophthalmology.

4.1 Results of vectorization of topological descriptors from persistence diagrams

As shown in Section 3.4, each eye fundus image is represented by a vector of 30 topological descriptors and then given to a machine learning classification algorithm to predict image quality for clinical use. Table 4.2 shows the resulting topological descriptors after the extraction and vectorization of the 30 topological indicators per image, as explained in Section 3.4.

Table 4.2: List of the 30 topological indicators calculated per image.

Variables 1-6	Variables 7-12	Variables 13-18	Variables 19-24	Variables 25-30
Persistence Entropy	2-Wasserstein Distance	Persistence Landscape	Betti Curve	Gaussian kernel
β_0	β_0	$L^2, k=1, \beta_0$	L^2, β_0	$L^2, \sigma=1.6, \beta_0$
Persistence Entropy	2-Wasserstein Distance	Persistence Landscape	Betti Curve	Gaussian kernel
β_1	β_1	$L^2, k=1, \beta_1$	L^2, β_1	$L^2, \sigma=1.6, \beta_1$
Bottleneck Distance	Persistence Landscape	Persistence Landscape	Gaussian kernel	Gaussian kernel
β_0	$L^1, k=1, \beta_0$	$L^2, k=2, \beta_0$	$L^1, \sigma=1.6, \beta_0$	$L^2, \sigma=3.2, \beta_0$
Bottleneck Distance	Persistence Landscape	Persistence Landscape	Gaussian kernel	Gaussian kernel
β_1	$L^1, k=1, \beta_1$	$L^2, k=2, \beta_1$	$L^1, \sigma=1.6, \beta_1$	$L^2, \sigma=3.2, \beta_1$
1-Wasserstein Distance	Persistence Landscape	Betti Curve	Gaussian kernel	Number of points in diagram
β_0	$L^1, k=2, \beta_0$	L^1, β_0	$L^1, \sigma=3.2, \beta_0$	β_0
1-Wasserstein Distance	Persistence Landscape	Betti Curve	Gaussian kernel	Number of points in diagram
β_1	$L^1, k=2, \beta_1$	L^1, β_1	$L^1, \sigma=3.2, \beta_1$	β_1

Preliminary explorations for the selection of a suitable algorithm were done on 6 classificators. Table 4.3 shows the performance metrics of the algorithms used in this phase. From these results 3 algorithms were selected for the next steps in the process: SVM, MLP, and LoGit .

Table 4.3: Performance metrics from classification algorithms initially evaluated.[1]

Model	AUC	CA	Precision	Recall	F1-Score
Support Vector Machine (SVM)	0.845	0.749	0.761	0.749	0.746
Decision Tree	0.870	0.894	0.895	0.894	0.894
k-Nearest Neighbors ($k-$NN)	0.941	0.898	0.900	0.898	0.898
Random Forest (RFC)	0.960	0.911	0.912	0.911	0.911
Logistic Regression (LoGit)	0.974	0.925	0.925	0.925	0.925
Multilayer Perceptron (MLP)	0.981	0.935	0.935	0.935	0.935

In the following step a fine-tuning of hyperparameters of the three selected algorithms was performed. Table 4.4 shows the resulting performance metrics after this

[1]Where: AUC = Area Under the Curve, and CA = Classification Accuracy.

process. Finally, the algorithm selected for the classification task was a LoGit because of the robust performance metrics in yielded and the relatively low computational cost when compared with both SVM and MLP.

Table 4.4: Performance metrics of fine tunned classification algorithms.

Algorithm	Precision Training Set	Precision Testing Set	Recall Training Set	Recall Testing Set	F1-Score Training Set	F1-Score Testing Set
SVM	0.961	0.957	0.961	0.957	0.961	0.957
MLP	0.910	0.930	0.910	0.930	0.910	0.930
LoGit	0.989	0.987	0.989	0.987	0.989	0.987

Table 4.5 shows the hyperparameters and values used for the tuning process for LoGit. The optimal results were obtained when Tolerance = 1e-08, C = 150000, Solver = liblinear, and Maximum iterations = 10000.

Table 4.5: Hyperparameters values for the tuning process of *LoGit*.

Parameter	Value
Tolerance	$\{1 \times 10^{-4}, 1 \times 10^{-6}, 1 \times 10^{-8}\}$
C	{50,000, 100,000, 150,000}
Solver	$\{lbfgs, saga, liblinear\}$
Maximum iterations	{10,000, 50,000, 100,000}

Once the LoGit was trained, it was tested on 600 images it had not previously classified. The results show consistency in the classification within classes as well as the global classification accuracy, as shown in Table 4.6. The Matthews correlation coefficient is also acceptable at 0.864, indicating consistent results in all the confusion matrix categories, as shown in Figure 4.1. Figure 4.2 shows the corresponding ROC curve.

Table 4.6: Classification report of *LoGit* with subset of not previously seen images.[2]

Label	Precision	Recall	F1-Score	Classification Accuracy	Count
good	0.912	0.952	0.932	0.932	294
bad	0.952	0.912	0.932		306

[2]Matthews correlation coefficient: 0.864.

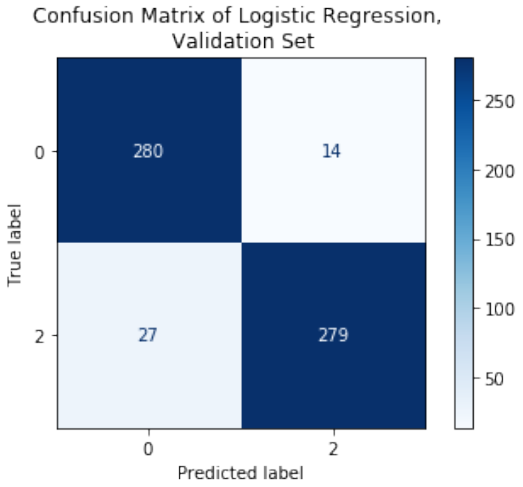

Figure 4.1: Confusion matrix of *LoGit* classification results on validation subset of 600 images.

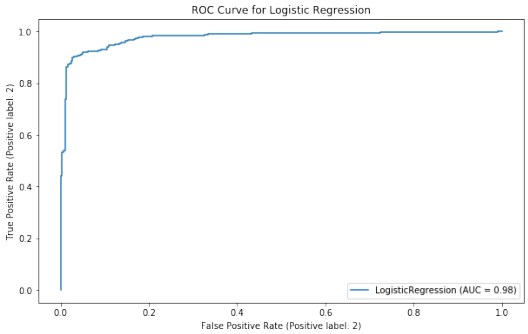

Figure 4.2: Receiver-operating characteristic curve for *LoGit* classification performance on validation subset of 600 images.

In order to bridge the numeric results to the clinical practice in the task of image quality assessment of eye fundus, a visualizatio of images adequately classified when compared to ground truth labels is presented in Figure 4.3. Figure 4.4 presents examples of images where *LoGit* wrongly classified them accroding to the ground truth.

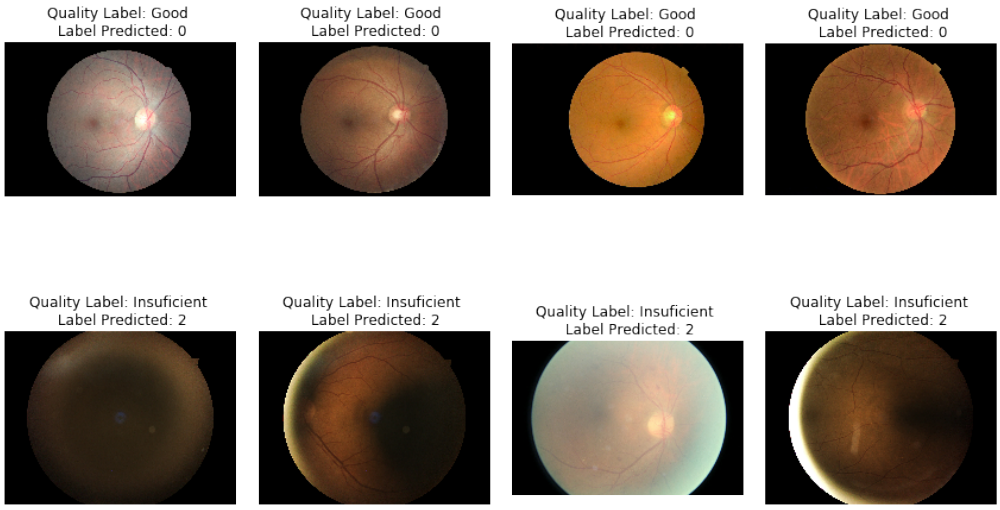

Figure 4.3: Subset of images **accurately** classified by *LoGit* algorithm when compared to ground truth labels. For labels predicted: $0 = good_quality$, $2 = not_enough_quality$

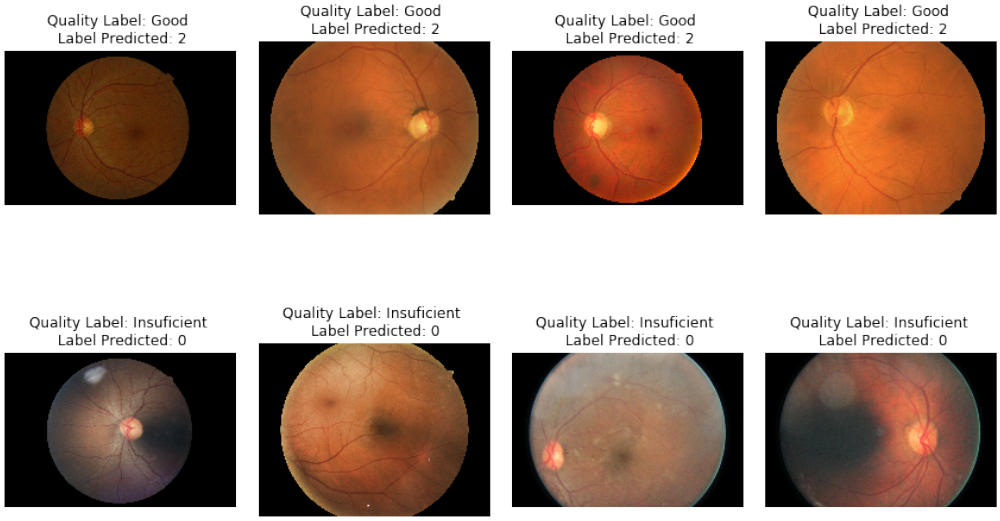

Figure 4.4: Subset of images **wrongly** classified by *LoGit* algorithm when compared to ground truth labels. For labels predicted: $0 = good_quality$, $2 = not_enough_quality$

On these visualizations it is apparent that the topological descriptors are robust to changes in color, illumination and blurring despite being vectors conformed by 30 elements, all derived from vectorizations of representations of persistence diagrams.

Chapter 5

Discussion and Conclusions

This chapter presents conclusions achieved based on the results reported in Chapter 4, and future work derived from the this project.

5.1 Discussion

Digital fundoscopy has become a valuable tool in the ophthalmic toolkit of the contemporary clinical practice. With the advent of telemedicine and electronic medical records [104], fundoscopy has moved to the mobile arena where now it is possible to perform it via smartphones [35, 105]. With these relatively new approaches reaching the clinical practice, computer aided diagnosis systems have also been proposed to assist the clinical process in situ or remotely [106, 107]. One of the first steps in the digital fundus image analysis pipeline is the quality assessment of the image obtained as presented in Section 2.3, this preprocessing step functions as a triage station allowing to filter out those images not meeting the minimum quality needed to continue for clinical use [47, 50, 52, 55]. This step is also performed by the clinician, but it is trivial for humans, given how the brain processes and understands images. For machines this step is fundamental and not trivial, since it will allow a smoother process down the pipeline of a CAD system.

As mentioned in Section 2.3, IQA techniques can be classified in three general groups, each representing the state of development in digital image analysis at the time of their publications (image characteristics, segmentation and deep learning). To the knowledge of the authors, this is the first work using Topological Data Analysis (TDA) to tackle the challenge of IQA in eye fundus images. The advantages of using TDA is that it represents less computational burden to the system, given that each image is first interpreted as a cubical complex and a cubical persistence calculation obtained represented by persistence diagrams, from which topological descriptors are extracted and vectorized. This allows to run the classification task not on an image matrix but on a vector much smaller than the input data. Therefore, TDA, for the context of IQA in eye fundus images, contributes with an inherent dimensionality reduction of

the data. This fact makes the method attractive specially for contexts where limited computational power is of significance like when clinicians integrate mobile devices or telemedicine to their practice.

Another beneficial contribution is that the topological descriptors seem to be able to capture enough data from the image that a relatively simple and computationally not demanding algorithm suffices to render results with robust classification metrics, this has also been observed by [108]. Figure 4.3 shows evidence to the idea presented in the previous sentence, where the images in the examples present variability in their color, illumination, blurring, and anatomical landmarks. Still the topological descriptors encapsule sufficient information for the classifier to perform robustly. For the instances where the classification is not appropriate, it seems that the localization of the optic nerve, as well as a significant proportion of irregularity in color distribution in the same image, as well as blurring could explain the errors, nevertheless more studies are needed in this direction to better understand this phenomenon.

Lastly, TDA seems to capture information in the form of topological descriptors that allows for the classification to perform close to the ground truth labels, which in the context of images from the clinical practice as is the EyePACS project, allows for the proposition of this method capturing information close to the way a clinician recollects image characteristics in order to decide if the image is of enough quality to be integrated in the clinical attention of the patient the data comes from.

5.2 Conclusions

By reviewing the available literature and looking to propose tools that are applicable to the clinical use, this work shows the implementation of TDA tools in the context of digital fundoscopy, from background segmentation to image quality assessment, where We propose a novel method for Image Quality Assessment of eye fundus images based on the extraction of topological descriptors integrated into a machine learning classifier. The classification metrics are robust and there is evidence that a topological approach facilitates the interpretation of the data in a similar way to how a clinician engages in these tasks during their practice. Further work is needed to investigate in more detail the clinical interpretations that might be suitable for the topological results obtained from eye fundus images. This could facilitate the use of TDA in later stages of the Computer Assisted Diagnosis pipeline in computational ophthalmological approaches. Also, a background segmentation method based in topological tools is presented, allowing for a potentially more agile preprocessing of the digital image, in preparation for clinical use down the analytical pipeline.

5.3 Future work

The natural development of this approach is to follow the way a clinician evaluates en eye fundus image, which is how the digital fundoscopy pipeline functions (Figure

2.16). Therefore approaches to integrate TDA into the stages of anatomical landmark location and characterization of patterns with correlation with pathologies are the logical extension of this work, either through complementing state of the art algorithms or assessing each stage from a completly topological paradigm. Independent of the particular approach taken, in order for these to function properly, Clinical pertinence must be included at the method development stages in order to keep the method multydisciplinary and with a high probability of applicability in a clinical setting.

5.4 Academic production and meetings attended

1. Published article:
    - Avilés-Rodríguez, G. J., Nieto-Hipólito, J. I., Cosío-León, M. D. L. Á., Romo-Cárdenas, G. S., Sánchez-López, J. D. D., Radilla-Chávez, P., & Vázquez-Briseño, M. (2021). Topological Data Analysis for Eye Fundus Image Quality Assessment. *Diagnostics*, 11(8), 1322.
2. Academic Meetings attended:
    - 5a Escuela de Análisis Topológico de Datos y Temas Relacionados, Figure 5.1.
        - November 19-23 2018.
        - Centro de Investigaciones en Matemáticas (CIMAT). Guanajuato, México.
        - Participant.
    - Técnicas y Herramientas de Inteligencia Artificial en Apoyo a la Investigación sobre Envejecimiento Saludable, Figure 5.2.
        - November 4-8 2019.
        - INAOE, Tonanzintla, Puebla, Mexico.
        - Presentation of poster.

Figure 5.1: Branding of the TDA school attended in 2018.

Figure 5.2: Branding of the fall school on AI tools for the support of research on healthy aging.

Bibliography

[1] Aditya Raj, Anil Kumar Tiwari, and Maria G Martini. Fundus image quality assessment: survey, challenges, and future scope. *IET Image Processing*, 13(8):1211–1224, 2019.

[2] Peter Densen. Challenges and opportunities facing medical education. *Transactions of the American Clinical and Climatological Association*, 122:48, 2011.

[3] Andrew J Blumberg and Michael A Mandell. Quantitative homotopy theory in topological data analysis. *Foundations of Computational Mathematics*, 13(6):885–911, 2013.

[4] Abolfazl Ramezanpour and Alireza Mashaghi. State assignment problem in systems biology and medicine: on the importance of state interaction network topology. *arXiv preprint arXiv:1705.02624*, 2017.

[5] Gunnar Carlsson. Topology and data. *Bulletin of the American Mathematical Society*, 46(2):255–308, 2009.

[6] Gunnar Carlsson and Mikael Vejdemo-Johansson. *Topological Data Analysis with Applications*. Cambridge University Press, 2021.

[7] Danijela Horak, Slobodan Maletić, and Milan Rajković. Persistent homology of complex networks. *Journal of Statistical Mechanics: Theory and Experiment*, 2009(03):P03034, 2009.

[8] Herbert Edelsbrunner, John Harer, et al. Persistent homology-a survey. *Contemporary mathematics*, 453:257–282, 2008.

[9] Afra Zomorodian and Gunnar Carlsson. Computing persistent homology. *Discrete & Computational Geometry*, 33(2):249–274, 2005.

[10] Charles Epstein, Gunnar Carlsson, and Herbert Edelsbrunner. Topological data analysis. *Inverse Problems*, 27(12):120201, 2011.

[11] Pek Y Lum, Gurjeet Singh, Alan Lehman, Tigran Ishkanov, Mikael Vejdemo-Johansson, Muthu Alagappan, John Carlsson, and Gunnar Carlsson. Extracting insights from the shape of complex data using topology. *Scientific reports*, 3(1):1–8, 2013.

[12] Gurjeet Singh, Facundo Memoli, Tigran Ishkhanov, Guillermo Sapiro, Gunnar Carlsson, and Dario L Ringach. Topological analysis of population activity in visual cortex. *Journal of vision*, 8(8):11–11, 2008.

[13] Yuri Dabaghian, Facundo Mémoli, Loren Frank, and Gunnar Carlsson. A topological paradigm for hippocampal spatial map formation using persistent homology. 2012.

[14] Moo K Chung, Peter Bubenik, and Peter T Kim. Persistence diagrams of cortical surface data. In *International Conference on Information Processing in Medical Imaging*, pages 386–397. Springer, 2009.

[15] Gurjeet Singh, Facundo Mémoli, Gunnar E Carlsson, et al. Topological methods for the analysis of high dimensional data sets and 3d object recognition. *PBG@ Eurographics*, 2, 2007.

[16] Jessica L Nielson, Jesse Paquette, Aiwen W Liu, Cristian F Guandique, C Amy Tovar, Tomoo Inoue, Karen-Amanda Irvine, John C Gensel, Jennifer Kloke, Tanya C Petrossian, et al. Topological data analysis for discovery in preclinical spinal cord injury and traumatic brain injury. *Nature communications*, 6(1):1–12, 2015.

[17] SN Deming, Y Michotte, Desiré Luc Massart, L Kaufman, and BGM Vandeginste. *Chemometrics: A textbook*. Elsevier, 1988.

[18] JL Aleixandre-Tudo, L Castello-Cogollos, JL Aleixandre, and R Aleixandre-Benavent. Chemometrics in food science and technology: A bibliometric study. *Chemometrics and Intelligent Laboratory Systems*, 222:104514, 2022.

[19] She-Gan Gao, Rui-Min Liu, Yun-Gang Zhao, Pei Wang, Douglas G Ward, Guang-Chao Wang, Xiang-Qian Guo, Juan Gu, Wan-Bin Niu, Tian Zhang, et al. Integrative topological analysis of mass spectrometry data reveals molecular features with clinical relevance in esophageal squamous cell carcinoma. *Scientific reports*, 6(1):1–12, 2016.

[20] Pablo G Camara, Daniel IS Rosenbloom, Kevin J Emmett, Arnold J Levine, and Raul Rabadan. Topological data analysis generates high-resolution, genome-wide maps of human recombination. *Cell systems*, 3(1):83–94, 2016.

[21] V Pedoia, J Haefeli, K Morioka, H-L Teng, L Nardo, RB Souza, AR Ferguson, and S Majumdar. Topological data analysis to predict cartilage lesion progression in knee osteoarthritis. *Osteoarthritis and Cartilage*, 25:S240–S241, 2017.

[22] Monica Nicolau, Arnold J Levine, and Gunnar Carlsson. Topology based data analysis identifies a subgroup of breast cancers with a unique mutational profile and excellent survival. *Proceedings of the National Academy of Sciences*, 108(17):7265–7270, 2011.

[23] Abasiofiok M Ibekwe, Jincai Ma, David E Crowley, Ching-Hong Yang, Alexis M Johnson, Tanya C Petrossian, and Pek Y Lum. Topological data analysis of escherichia coli o157: H7 and non-o157 survival in soils. *Frontiers in cellular and infection microbiology*, 4:122, 2014.

[24] Kathryn Garside, Robin Henderson, Irina Makarenko, and Cristina Masoller. Topological data analysis of high resolution diabetic retinopathy images. *PloS one*, 14(5):e0217413, 2019.

[25] Attila Budai, Rüdiger Bock, Andreas Maier, Joachim Hornegger, and Georg Michelson. Robust vessel segmentation in fundus images. *International journal of biomedical imaging*, 2013, 2013.

[26] Talha Qaiser, Yee-Wah Tsang, Daiki Taniyama, Naoya Sakamoto, Kazuaki Nakane, David Epstein, and Nasir Rajpoot. Fast and accurate tumor segmentation of histology images using persistent homology and deep convolutional features. *Medical image analysis*, 55:1–14, 2019.

[27] Talha Qaiser, Korsuk Sirinukunwattana, Kazuaki Nakane, Yee-Wah Tsang, David Epstein, and Nasir Rajpoot. Persistent homology for fast tumor segmentation in whole slide histology images. *Procedia Computer Science*, 90:119–124, 2016.

[28] Talha Qaiser, Yee-Wah Tsang, David Epstein, and Nasir Rajpoot. Tumor segmentation in whole slide images using persistent homology and deep convolutional features. In *Annual Conference on Medical Image Understanding and Analysis*, pages 320–329. Springer, 2017.

[29] Emanuele Trucco, Tom MacGillivray, and Yanwu Xu. *Computational retinal image analysis: Tools, applications and perspectives*. Academic Press, 2019.

[30] Matthew J Burton, Hannah B Faal, Jacqueline Ramke, Thulasiraj Ravilla, Peter Holland, Ningli Wang, Sheila K West, Rupert RA Bourne, Nathan G Congdon, and Allen Foster. Announcing the lancet global health commission on global eye health. *The Lancet Global Health*, 7(12):e1612–e1613, 2019.

[31] Rupert RA Bourne, Seth R Flaxman, Tasanee Braithwaite, Maria V Cicinelli, Aditi Das, Jost B Jonas, Jill Keeffe, John H Kempen, Janet Leasher, Hans Limburg, et al. Magnitude, temporal trends, and projections of the global prevalence of blindness and distance and near vision impairment: a systematic review and meta-analysis. *The Lancet Global Health*, 5(9):e888–e897, 2017.

[32] Adam Gordois, Henry Cutler, Lynne Pezzullo, Keith Gordon, Alan Cruess, Steve Winyard, Wanda Hamilton, and Kathleen Chua. An estimation of the worldwide economic and health burden of visual impairment. *Global public health*, 7(5):465–481, 2012.

[33] World Health Organization et al. World report on vision. 2019.

[34] Gerardo Heinze, Víctor Hugo Olmedo Canchola, Germán Bazán Miranda, Napoléon Andrés Bernard Fuentes, and Diana Patricia Guízar Sánchez. Los médicos especialistas en méxico. *Gaceta médica de México*, 154(3):342–351, 2018.

[35] Hillary K Rono, Andrew Bastawrous, David Macleod, Emmanuel Wanjala, Gian Luca Di Tanna, Helen A Weiss, and Matthew J Burton. Smartphone-based screening for visual impairment in kenyan school children: a cluster randomised controlled trial. *The Lancet Global Health*, 6(8):e924–e932, 2018.

[36] Muthu Rama Krishnan Mookiah, U Rajendra Acharya, Chua Kuang Chua, Choo Min Lim, EYK Ng, and Augustinus Laude. Computer-aided diagnosis of diabetic retinopathy: A review. *Computers in biology and medicine*, 43(12):2136–2155, 2013.

[37] Myron Yanoff. *Ophthalmic diagnosis & treatment*. JP Medical Ltd, 2014.

[38] Beau B Bruce. Examining the ocular fundus and interpreting what you see. *The American Academy of Neurology Institute: Minneapolis, MN, USA*, 2017.

[39] Stanford Medicine 25. Fundoscopic exam (ophthalmoscopy).

[40] Varun Gulshan, Lily Peng, Marc Coram, Martin C Stumpe, Derek Wu, Arunachalam Narayanaswamy, Subhashini Venugopalan, Kasumi Widner, Tom Madams, Jorge Cuadros, et al. Development and validation of a deep learning algorithm for detection of diabetic retinopathy in retinal fundus photographs. *Jama*, 316(22):2402–2410, 2016.

[41] Mike Voets, Kajsa Møllersen, and Lars Ailo Bongo. Reproduction study using public data of: Development and validation of a deep learning algorithm for detection of diabetic retinopathy in retinal fundus photographs. *PloS one*, 14(6):e0217541, 2019.

[42] Jaemin Son, Joo Young Shin, Hoon Dong Kim, Kyu-Hwan Jung, Kyu Hyung Park, and Sang Jun Park. Development and validation of deep learning models for screening multiple abnormal findings in retinal fundus images. *Ophthalmology*, 127(1):85–94, 2020.

[43] Jonathan Krause, Varun Gulshan, Ehsan Rahimy, Peter Karth, Kasumi Widner, Greg S Corrado, Lily Peng, and Dale R Webster. Grader variability and the importance of reference standards for evaluating machine learning models for diabetic retinopathy. *Ophthalmology*, 125(8):1264–1272, 2018.

[44] Muhammad Imran Razzak, Saeeda Naz, and Ahmad Zaib. Deep learning for medical image processing: Overview, challenges and the future. *Classification in BioApps*, pages 323–350, 2018.

[45] Michael D Abràmoff, Mona K Garvin, and Milan Sonka. Retinal imaging and image analysis. *IEEE reviews in biomedical engineering*, 3:169–208, 2010.

[46] Rui Bernardes, Pedro Serranho, and Conceição Lobo. Digital ocular fundus imaging: a review. *Ophthalmologica*, 226(4):161–181, 2011.

[47] Marc Lalonde, Langis Gagnon, Marie-Carole Boucher, et al. Automatic visual quality assessment in optical fundus images. In *Proceedings of vision interface*, volume 32, pages 259–264. Ottawa, 2001.

[48] Herbert Davis, Stephen Russell, Eduardo Barriga, Michael Abramoff, and Peter Soliz. Vision-based, real-time retinal image quality assessment. In *2009 22nd IEEE International Symposium on Computer-Based Medical Systems*, pages 1–6. IEEE, 2009.

[49] Alan D Fleming, Sam Philip, Keith A Goatman, John A Olson, and Peter F Sharp. Automated assessment of diabetic retinal image quality based on clarity and field definition. *Investigative ophthalmology & visual science*, 47(3):1120–1125, 2006.

[50] João Miguel Pires Dias, Carlos Manta Oliveira, and Luis A da Silva Cruz. Retinal image quality assessment using generic image quality indicators. *Information Fusion*, 19:73–90, 2014.

[51] Samuel C Lee and Yiming Wang. Automatic retinal image quality assessment and enhancement. In *Medical imaging 1999: image processing*, volume 3661, pages 1581–1590. International Society for Optics and Photonics, 1999.

[52] Herman Bartling, Peter Wanger, and Lene Martin. Automated quality evaluation of digital fundus photographs. *Acta ophthalmologica*, 87(6):643–647, 2009.

[53] Meindert Niemeijer, Michael D Abramoff, and Bram van Ginneken. Image structure clustering for image quality verification of color retina images in diabetic retinopathy screening. *Medical image analysis*, 10(6):888–898, 2006.

[54] RA Welikala, MM Fraz, PJ Foster, PH Whincup, Alicja R Rudnicka, Christopher G Owen, DP Strachan, Sarah A Barman, et al. Automated retinal image quality assessment on the uk biobank dataset for epidemiological studies. *Computers in biology and medicine*, 71:67–76, 2016.

[55] Dwarikanath Mahapatra, Pallab K Roy, Suman Sedai, and Rahil Garnavi. Retinal image quality classification using saliency maps and cnns. In *International Workshop on Machine Learning in Medical Imaging*, pages 172–179. Springer, 2016.

[56] DB Usher, M Himaga, MJ Dumskyj, and JF Boyce. Automated assessment of digital fundus image quality using detected vessel area. In *Proceedings of Medical Image Understanding and Analysis*, pages 81–84. Citeseer, 2003.

[57] Andrew Hunter, James A Lowell, Maged Habib, Bob Ryder, Ansu Basu, and David Steel. An automated retinal image quality grading algorithm. In *2011 Annual International Conference of the IEEE Engineering in Medicine and Biology Society*, pages 5955–5958. IEEE, 2011.

[58] Thomas Köhler, Attila Budai, Martin F Kraus, Jan Odstrčilik, Georg Michelson, and Joachim Hornegger. Automatic no-reference quality assessment for retinal fundus images using vessel segmentation. In *Proceedings of the 26th IEEE international symposium on computer-based medical systems*, pages 95–100. IEEE, 2013.

[59] Hanung Adi Nugroho, Titin Yulianti, Noor Akhmad Setiawan, and Dhimas Arief Dharmawan. Contrast measurement for no-reference retinal image quality assessment. In *2014 6th International Conference on Information Technology and Electrical Engineering (ICITEE)*, pages 1–4. IEEE, 2014.

[60] Luca Giancardo, Michael D Abràmoff, E Chaum, TP Karnowski, F Meriaudeau, and KW Tobin. Elliptical local vessel density: a fast and robust quality metric for retinal images. In *2008 30th Annual International Conference of the IEEE Engineering in Medicine and Biology Society*, pages 3534–3537. IEEE, 2008.

[61] Jan Paulus, Jörg Meier, Rüdiger Bock, Joachim Hornegger, and Georg Michelson. Automated quality assessment of retinal fundus photos. *International journal of computer assisted radiology and surgery*, 5(6):557–564, 2010.

[62] Ramon Pires, Herbert F Jelinek, Jacques Wainer, and Anderson Rocha. Retinal image quality analysis for automatic diabetic retinopathy detection. In *2012 25th SIBGRAPI Conference on Graphics, Patterns and Images*, pages 229–236. IEEE, 2012.

[63] Honggang Yu, Carla Agurto, Simon Barriga, Sheila C Nemeth, Peter Soliz, and Gilberto Zamora. Automated image quality evaluation of retinal fundus photographs in diabetic retinopathy screening. In *2012 IEEE Southwest symposium on image analysis and interpretation*, pages 125–128. IEEE, 2012.

[64] Gajendra Jung Katuwal, John Kerekes, Rajeev Ramchandran, Christye Sisson, and Navalgund Rao. Automatic fundus image field detection and quality assessment. In *2013 IEEE Western New York Image Processing Workshop (WNYIPW)*, pages 9–13. IEEE, 2013.

[65] Fengshou Yin, Damon Wing Kee Wong, Ai Ping Yow, Beng Hai Lee, Ying Quan, Zhuo Zhang, Kavitha Gopalakrishnan, Ruoying Li, and Jiang Liu. Automatic

retinal interest evaluation system (aries). In *2014 36th Annual International Conference of the IEEE Engineering in Medicine and Biology Society*, pages 162–165. IEEE, 2014.

[66] Diana Veiga, Carla Pereira, Manuel João Ferreira, Luís Gonçalves, and João Monteiro. Quality evaluation of digital fundus images through combined measures. *Journal of Medical Imaging*, 1(1):014001, 2014.

[67] Zhenjie Yao, Zhipeng Zhang, Li-Qun Xu, Qingxia Fan, and Ling Xu. Generic features for fundus image quality evaluation. In *2016 IEEE 18th International Conference on e-Health Networking, Applications and Services (Healthcom)*, pages 1–6. IEEE, 2016.

[68] Shaoze Wang, Kai Jin, Haitong Lu, Chuming Cheng, Juan Ye, and Dahong Qian. Human visual system-based fundus image quality assessment of portable fundus camera photographs. *IEEE transactions on medical imaging*, 35(4):1046–1055, 2015.

[69] Feng Shao, Yan Yang, Qiuping Jiang, Gangyi Jiang, and Yo-Sung Ho. Automated quality assessment of fundus images via analysis of illumination, naturalness and structure. *IEEE Access*, 6:806–817, 2017.

[70] Dwarikanath Mahapatra, Pallab K Roy, Suman Sedai, and Rahil Garnavi. A cnn based neurobiology inspired approach for retinal image quality assessment. In *2016 38th Annual International Conference of the IEEE Engineering in Medicine and Biology Society (EMBC)*, pages 1304–1307. IEEE, 2016.

[71] FengLi Yu, Jing Sun, Annan Li, Jun Cheng, Cheng Wan, and Jiang Liu. Image quality classification for dr screening using deep learning. In *2017 39th Annual International Conference of the IEEE Engineering in Medicine and Biology Society (EMBC)*, pages 664–667. IEEE, 2017.

[72] James R Munkres. *Elements of algebraic topology*. CRC press, 2018.

[73] Herbert Edelsbrunner and John Harer. *Computational topology: an introduction*. American Mathematical Soc., 2010.

[74] Frédéric Chazal and Bertrand Michel. An introduction to topological data analysis: fundamental and practical aspects for data scientists. *Frontiers in Artificial Intelligence*, 4, 2021.

[75] Afra J Zomorodian. *Topology for computing*, volume 16. Cambridge university press, 2005.

[76] Tinne Hoff Kjeldsen. History of convexity and mathematical programming: Connections and relationships in two episodes of research in pure and applied mathematics of the 20th century. In *Proceedings of the International Congress of Mathematicians 2010 (ICM 2010) (In 4 Volumes) Vol. I: Plenary Lectures and Ceremonies Vols. II–IV: Invited Lectures*, pages 3233–3257. World Scientific, 2010.

[77] Contributors Wikipedia. Convex hull, Sep 2018.

[78] Frédéric Chazal and Bertrand Michel. An introduction to topological data analysis: fundamental and practical aspects for data scientists. *arXiv preprint arXiv:1710.04019*, 2017.

[79] Robert W Ghrist. *Elementary applied topology*, volume 1. Createspace Seattle, 2014.

[80] Bastian Rieck. *Persistent Homology in Multivariate Data Visualization*. PhD thesis, Ruprecht-Karls-Universität Heidelberg, 2017.

[81] Georges Voronoi. Nouvelles applications des paramètres continus à la théorie des formes quadratiques. premier mémoire. sur quelques propriétés des formes quadratiques positives parfaites. *Journal für die reine und angewandte Mathematik (Crelles Journal)*, 1908(133):97–102, 1908.

[82] Vin De Silva. A weak definition of delaunay triangulation. *arXiv preprint cs/0310031*, 2003.

[83] Jorge Cuadros and George Bresnick. Eyepacs: an adaptable telemedicine system for diabetic retinopathy screening. *Journal of diabetes science and technology*, 3(3):509–516, 2009.

[84] Etienne Decencière, Xiwei Zhang, Guy Cazuguel, Bruno Lay, Béatrice Cochener, Caroline Trone, Philippe Gain, Richard Ordonez, Pascale Massin, Ali Erginay, Béatrice Charton, and Jean-Claude Klein. Feedback on a publicly distributed database: the messidor database. *Image Analysis & Stereology*, 33(3):231–234, August 2014.

[85] Aptos 2019 diabetic retinopathy dataset.

[86] Huazhu Fu, Boyang Wang, Jianbing Shen, Shanshan Cui, Yanwu Xu, Jiang Liu, and Ling Shao. Evaluation of retinal image quality assessment networks in different color-spaces. In *International Conference on Medical Image Computing and Computer-Assisted Intervention*, pages 48–56. Springer, 2019.

[87] Andrés D Pérez, Oscar Perdomo, and Fabio A González. A lightweight deep learning model for mobile eye fundus image quality assessment. In *15th International Symposium on Medical Information Processing and Analysis*, volume 11330, page 113300K. International Society for Optics and Photonics, 2020.

[88] Afra Zomorodian. Topological data analysis. *Advances in applied and computational topology*, 70:1–39, 2012.

[89] Marc Niethammer, Andrew N Stein, William D Kalies, Pawel Pilarczyk, Konstantin Mischaikow, and Allen Tannenbaum. Analysis of blood vessel topology by cubical homology. In *Proceedings. International Conference on Image Processing*, volume 2, pages II–II. IEEE, 2002.

[90] Paweł Pilarczyk and Pedro Real. Computation of cubical homology, cohomology, and (co) homological operations via chain contraction. *Advances in Computational Mathematics*, 41(1):253–275, 2015.

[91] Petre Stoica, Randolph L Moses, et al. Spectral analysis of signals. 2005.

[92] Hetal J Vala and Astha Baxi. A review on otsu image segmentation algorithm. *International Journal of Advanced Research in Computer Engineering & Technology (IJARCET)*, 2(2):387–389, 2013.

[93] Kangning Li and Yunhao Chen. A genetic algorithm-based urban cluster automatic threshold method by combining viirs dnb, ndvi, and ndbi to monitor urbanization. *Remote Sensing*, 10(2):277, 2018.

[94] Juan Miguel Valverde Martínez. Laid/otsu.py at master · jmlipman/laid · github. `https://github.com/jmlipman/LAID/blob/master/IP/Otsu/otsu.py`. (Accessed on 04/29/2020).

[95] Hubert Wagner, Chao Chen, and Erald Vuçini. Efficient computation of persistent homology for cubical data. In *Topological methods in data analysis and visualization II*, pages 91–106. Springer, 2012.

[96] Alon Efrat, Alon Itai, and Matthew J Katz. Geometry helps in bottleneck matching and related problems. *Algorithmica*, 31(1):1–28, 2001.

[97] Michael Kerber, Dmitriy Morozov, and Arnur Nigmetov. Geometry helps to compare persistence diagrams, 2017.

[98] Peter Bubenik et al. Statistical topological data analysis using persistence landscapes. *J. Mach. Learn. Res.*, 16(1):77–102, 2015.

[99] Peter Bubenik and Paweł Dłotko. A persistence landscapes toolbox for topological statistics. *Journal of Symbolic Computation*, 78:91–114, 2017.

[100] Jan Reininghaus, Stefan Huber, Ulrich Bauer, and Roland Kwitt. A stable multiscale kernel for topological machine learning. In *Proceedings of the IEEE conference on computer vision and pattern recognition*, pages 4741–4748, 2015.

[101] Janez Demšar, Tomaž Curk, Aleš Erjavec, Črt Gorup, Tomaž Hočevar, Mitar Milutinovič, Martin Možina, Matija Polajnar, Marko Toplak, Anže Starič, et al. Orange: data mining toolbox in python. *the Journal of machine Learning research*, 14(1):2349–2353, 2013.

[102] Yasen Jiao and Pufeng Du. Performance measures in evaluating machine learning based bioinformatics predictors for classifications. *Quantitative Biology*, 4(4):320–330, 2016.

[103] Davide Chicco and Giuseppe Jurman. The advantages of the matthews correlation coefficient (mcc) over f1 score and accuracy in binary classification evaluation. *BMC genomics*, 21(1):1–13, 2020.

[104] Peter W DeBry. Considerations for choosing an electronic medical record for an ophthalmology practice. *Archives of ophthalmology*, 119(4):590–596, 2001.

[105] Anita Barikian and Luis J Haddock. Smartphone assisted fundus fundoscopy-/photography. *Current Ophthalmology Reports*, 6(1):46–52, 2018.

[106] Marta Díez-Sotelo, Macarena Díaz, Maximino Abraldes, Francisco Gómez-Ulla, Manuel G Penedo, and Marcos Ortega. A novel automatic method to estimate visual acuity and analyze the retinal vasculature in retinal vein occlusion using swept source optical coherence tomography angiography. *Journal of Clinical Medicine*, 8(10):1515, 2019.

[107] Muhammad Arsalan, Muhammad Owais, Tahir Mahmood, Se Woon Cho, and Kang Ryoung Park. Aiding the diagnosis of diabetic and hypertensive retinopathy using artificial intelligence-based semantic segmentation. *Journal of clinical medicine*, 8(9):1446, 2019.

[108] Valente López-Reyes, MA Cosío-León, GJ Avilés-Rodríguez, Anabel Martínez-Vargas, and G Romo-Cárdenas. A topological approach for the pattern analysis on chest x-ray images of covid-19 patients. In *Medical Imaging 2021: Physics of Medical Imaging*, volume 11595, page 115954C. International Society for Optics and Photonics, 2021.